Insights into the single particle composition, size, mixing state and aspect ratio of freshly emitted mineral dust from field measurements in the Moroccan Sahara using electron microscopy

Agnesh Panta[1], Konrad Kandler[1], Andres Alastuey[2], Cristina González-Flórez[3], Adolfo González-Romero[2,3], Martina Klose[4], Xavier Querol[2], Cristina Reche[2], Jesús Yus-Díez[2,5,a], and Carlos Pérez García-Pando[3,6]

[1]Atmospheric Aerosol Group, Institute of Applied Geosciences, Technical University of Darmstadt, Darmstadt, Germany
[2]Institute of Environmental Assessment and Water Research (IDAEA-CSIC), Barcelona, 08034, Spain
[3]Barcelona Supercomputing Center, Barcelona, Spain
[4]Department Troposphere Research, Institute of Meteorology and Climate Research (IMK-TRO), Karlsruhe Institute of Technology (KIT), Karlsruhe, Germany
[5]Grup de Meteorologia, Departament de Física Aplicada, Universitat de Barcelona, C/Martí i Franquès, 1, 08028, Barcelona, Spain
[6]ICREA, Catalan Institution for Research and Advanced Studies, Barcelona, Spain
[a]now at: Center for Atmospheric Research, University of Nova Gorica, Vipavska 11c, SI-5270 Ajdovščina, Slovenia

Correspondence: Agnesh Panta (agnesh@geo.tu-darmstadt.de)

Abstract.

The chemical and morphological properties of mineral dust aerosols emitted by wind erosion from arid and semi-arid regions influence climate, ocean and land ecosystems, air quality, and multiple socio-economic sectors. However, there is an incomplete understanding of the emitted dust particle size distribution (PSD) in terms of its constituent minerals that typically result from the fragmentation of soil aggregates during wind erosion. The emitted dust PSD affects the duration of particle transport and thus each mineral's global distribution, along with its specific effect upon climate. This lack of understanding is largely due to the scarcity of relevant in situ measurements in dust sources. To advance our understanding of the physicochemical properties of the emitted dust PSD, we present insights into the elemental composition and morphology of individual dust particles collected during the FRontiers in dust minerAloGical coMposition and its Effects upoN climaTe (FRAGMENT) field campaign in the Moroccan Sahara in September 2019. We analyzed more than 300,000 freshly emitted individual particles by performing offline analysis in the laboratory using Scanning Electron Microscopy (SEM) coupled with Energy-Dispersive X-ray Spectrometry (EDX). Eight major particle-type classes were identified ~~where clay minerals make~~ with clay minerals making up the majority of the analyzed particles ~~by number, with carbonates and quartz contributing~~ both by number and mass, followed by quartz whereas carbonates and feldspar contributed to a lesser extent. We provide an exhaustive analysis of the ~~size distribution~~ PSD and potential mixing state of different particle types, focusing largely on iron-rich (Fe-oxi/hydroxides) and feldspar particles, which are key to the effects of dust upon radiation and clouds, respectively. Nearly pure or externally mixed Fe-oxi/hydroxides are present ~~only~~ mostly in diameters smaller than 2 μm ~~and mainly~~ with the highest fraction below 1 μm at about 3.75 % abundance by mass. Fe-oxi/hydroxides tend to be increasingly internally mixed with other minerals,

especially clays, as particle size increases, i.e., the volume fraction of Fe-oxi/hydroxides in aggregates decreases with particle size. Pure (externally-mixed) feldspar represented ~~3.7~~ 3.2 % of all the particles by mass, of which we estimated about a ~~quarter~~ tenth to be K-feldspar. The externally-mixed total feldspar and K-feldspar abundances are relatively invariant with particle size, in contrast to the increasing abundance of feldspar-like (internally-mixed) aggregates with particle size with mass fractions ranging from 5 to 18 %. We also found that overall the median aspect ratio is rather constant across particle size and mineral groups, although we obtain slightly higher aspect ratios for internally-mixed particles. The detailed information on the composition of freshly emitted individual dust particles along with the quantitative analysis of their mixing state presented here can be used to constrain climate models including mineral species in their representation of the dust cycle.

1 Introduction

Mineral dust, as one of the most important natural aerosols in the atmosphere, is a key player in influencing the global climate system (Shao et al., 2011). It is the most abundant aerosol type in terms of ~~dry~~ mass (Choobari et al., 2014; Textor et al., 2006), with an estimated emission flux between 3400 and 8900 Tg yr^{-1} for particles smaller than 20 μm geometric diameter (Kok et al., 2022). In particular, Northern Africa is responsible for an estimated 50 % of global windblown mineral dust emissions (Engelstaedter et al., 2006; Kok et al., 2021). Dust affects directly the Earth's radiative budget via scattering and absorption of radiation (Sokolik et al., 2001; Pérez et al., 2006; Strong et al., 2018), and indirectly by influencing cloud development on a microphysical level by acting as cloud condensation nuclei and ice nuclei (Zimmermann et al., 2008; Kumar et al., 2011; Hoose and Möhler, 2012; Froyd et al., 2022), and thus impacting cloud optical properties and radiation. Once uplifted over the source areas, dust can travel thousands of kilometers away from these and can act as a carrier for micronutrients, such as iron and phosphorous, to the ocean (Jickells et al., 2005; Schulz et al., 2012; Rodríguez et al., 2021; Myriokefalitakis et al., 2022) and the Amazon rainforest (Yu et al., 2015), with implications for biogeochemical cycles and ocean uptake of atmospheric carbon dioxide by promoting phytoplankton growth (Mahowald et al., 2009). Additionally, dust can be deposited on snow or ice thereby reducing snow/ice reflectance (surface darkening) and consequently changing the climate and water cycle by accelerating snow melting (Painter et al., 2010; Sarangi et al., 2020). Dust can also interact with air pollutants by acting as a ~~catalyzer~~ catalyst and providing a surface for heterogeneous reactions (Cwiertny et al., 2008; Ndour et al., 2008). Finally, dust might negatively impact human health (Querol et al., 2019; Pérez García-Pando et al., 2014; Giannadaki et al., 2014), induce a decrease in solar energy yield by dust deposition to solar panels (Piedra and Moosmüller, 2017), and negatively impact aircraft operations due to reduced visibility (Middleton, 2017; Monteiro et al., 2022). Most of these processes rely not only on the total mass of dust but also on its microphysical properties and mineral composition (Mahowald et al., 2014).

The physicochemical properties of mineral dust aerosols including their particle size distribution (PSD), composition, mixing state and shape determine their impact on climate and atmospheric chemistry (Formenti et al., 2011). The emitted PSD, spanning from a few nanometers to hundreds of micrometers, is critical in constraining the dust atmospheric lifetime, as coarser particles tend to deposit ~~quickly~~ faster due to gravity, albeit less than previously thought ~~(van der Does et al., 2018; Adebiyi and Kok, 2020; ?)~~ (van der Does et al., 2018; Adebiyi and Kok, 2020; Adebiyi et al., 2023). The chemical and mineralogical composition is an-

other key factor to consider; for example, the absorption properties and ice-nucleating ability of dust depend upon its mineralogy, mainly upon the presence of iron oxides (Li et al., 2021) and K-feldspar (Atkinson et al., 2013; Kiselev et al., 2017; Welti et al., 2019; Yun et al., 2020), respectively. The mixing or aggregation state of the different dust minerals is also important in determining the behavior of dust in the atmosphere in terms of its reactivity, chemical processing, optical properties, ice nucleation ability and dust deposition (Fitzgerald et al., 2015; Kandler et al., 2018). For example, dust is more optically absorbing when iron oxides are internally mixed with other minerals than when they are externally mixed (Sokolik and Toon, 1999). The feldspar fraction in desert soils also varies considerably. In parts of northern Africa (southern Algeria, northern Mauritania and northern Niger) it can reach $\sim$ 12 to 20 % whereas, in western Sahel, the feldspar fraction is less than 2% (Nickovic et al., 2012; Perlwitz et al., 2015a). In addition, the ice nucleation property of mineral dust depends not only on the source ~~region~~ composition but also on the feldspar ~~size distribution~~PSD, which among other aspects, dictates its lifetime in the atmosphere. Moreover, the ice-nucleating ~~property~~ properties of K-feldspar ~~varies~~ vary significantly despite having a comparable crystal structure and composition, leading to a variety of ice-nucleating abilities (Harrison et al., 2016). K-feldspar also dominates the number of ice nuclei in both the internally mixed and externally mixed cases (Atkinson et al., 2013). Particle shape influences the dust single-scattering properties (Lindqvist et al., 2014; Nousiainen and Kandler, 2015; Saito and Yang, 2021). Accurate quantification of dust shape is important for calculating the dust impact on radiative forcing (Ito et al., 2021) and the terminal velocity of dust particles (Ginoux, 2003; Huang et al., 2020), albeit with high uncertainties for both of these effects (Nousiainen et al., 2011). Mineral dust also contributes significantly to the atmospheric aerosol mass loadings, which are retrieved from satellite measurements and ground-based lidar measurements applying algorithms that use particle shape as one of the input parameters (Dubovik et al., 2006; Gliß et al., 2021). The importance of realistic size equivalence and shape of spheroidal Saharan dust particles on optical properties and the radiative effect was studied in Otto et al. (2011) with data gathered during SAMUM-1 in Morocco. Furthermore, scanning electron microscopy (SEM) was used to characterize the mineralogical composition and shape of mineral dust particles collected during the SAMUM campaign over Morocco in 2006 (Lindqvist et al., 2014). They found great variation between the scattering properties of spheres, spheroids, and mineral dust particles characterized by SEM (Lindqvist et al., 2014). Moreover, for non-symmetrical particles, a preferential orientation in the atmosphere is observed where a shape-dependent settling behavior comes into effect (Li and Osada, 2007). There is also a shape-dependent separation of mineral dust into layers of different altitudes during cross-Atlantic transport of Saharan dust which strongly points to a shape-preferential settling of particles (Yang et al., 2013). In addition, dust nonsphericity could enhance the snow albedo reduction by up to 20 % relative to spherical dust (Shi et al., 2022). As the shape of dust particles is highly aspherical (Huang et al., 2020), this can further influence their optical properties (Ito et al., 2021; Otto et al., 2009; Mishchenko et al., 1997; Nousiainen and Kandler, 2015; Klose et al., 2021). Finally, the dust lifetime in the atmosphere is also affected by particle shape and density (which depends on mineralogy), with more spherical and denser particles being deposited faster (Huang et al., 2020; Mallios et al., 2020). Other potentially important aspects that have been largely unexplored are the potential interdependencies among particle size, composition, mixing state, and shape. For example, while it is well known that composition is size-dependent (Kandler et al., 2009, 2011; Ryder et al., 2018; Liu et al., 2018), very little is known about the potential dependencies of shape and mixing state upon both particle composition and size.

Models that include spatiotemporal variations in mineralogical composition of windblown dust are relatively new (Perlwitz et al., 2015a, b; Scanza et al., 2015) and currently use rather crude soil mineralogy maps (Claquin et al., 1999; Nickovic et al., 2012; Journet et al., 2014) as a lower boundary condition. Soil mineralogy maps are based on massive extrapolation from a limited amount of soil mineralogical analyses, ancillary information on soil texture and color, and several additional assumptions. This limited knowledge together with our incomplete understanding and scarcity of measurements on the emitted dust physicochemical properties and their relationship with the PSD and composition of the parent soil precludes accurate model assessment of the effects of dust upon climate (Perlwitz et al., 2015a; Pérez García-Pando et al., 2016; Li et al., 2021). ~~One reason for such measurement scarcity is that sourceareas, particularly the host prolific ones, are typically located in remote areas and subject to harsh conditions~~However, despite their importance, there exist very few ground based in situ measurement studies to characterize the particle composition and microphysical properties. This is mainly due to the difficulty in dust sampling at source, as source areas are often remote harsh environments. Also, frequent dust storms ~~can lead to large dust concentrations posing a great challenge to sample for single-particle analysis as the filter can be quickly overloaded~~result in high particulate concentrations and filter overload, providing a challenge to analyze by automated SEM.

In this contribution, we investigate the size, morphology, elemental (and mineralogical) composition, and mixing state of freshly emitted individual dust particles based on samples collected during a major wind erosion and dust emission field campaign in the Moroccan Sahara within the framework of the FRontiers in dust minerAloGical coMposition and its Effects upoN climate (FRAGMENT) project. Three different ~~sampling~~ instruments were used to ~~collect freshly emitted mineral dustparticles and the~~ sample mineral dust, for the measurement of chemical and physical properties of individual dust particles ~~were examined in detail using~~ by SEM coupled with an energy-dispersive X-ray ~~analysis~~ analyzer (EDX). Our detailed chemical and physical speciation represent a first step towards advancing our knowledge on the emitted PSD of individual dust minerals ~~,~~ that will ultimately help understanding the relationship between the size-resolved composition of the emitted dust and that of the parent soil. Such knowledge is needed to better constrain climate models that ~~are starting to~~ consider mineralogical variations in their representation of the dust cycle (Perlwitz et al., 2015a; Scanza et al., 2015; Li et al., 2021)~~, and it~~ . This is timely given the prospect of global soil mineralogy retrievals using high-quality spaceborne hyperspectral measurements (Green et al., 2020).

2 Materials and methods

2.1 Measurement site

In situ aerosol sampling was conducted in a small study area in SE Morocco during FRAGMENT wind erosion and dust emission field campaign between 03 September and 01 October 2019. A suite of meteorological and aerosol instruments was deployed as depicted in Fig. 1 to measure key meteorological and aerosol quantities. Below we describe only the instruments and measurements used in this contribution. Measurements performed during the campaign with other instruments displayed in Fig. 1b are discussed in companion papers (González-Flórez et al., 2022; Yus-Díez et al., in prep.). The study area, locally known as L'Bour (29°49'30" N, 5°52'25" W $\approx$ 500 m a.s.l.), is a small ephemeral lake located in the Lower Drâa Valley of

Morocco and lies at the edge of the Saharan Desert approximately 15 km to the west of the small village M'Hamid El Ghizlane. The region is characterized by high aerosol optical depth (Ginoux et al., 2012). The location was chosen primarily based on its dust emission potential and logistical feasibility. L'Bour is approximately flat and devoid of vegetation or other obstacles within a radius of $\sim$1 km and is surrounded by small sand dune fields. The surface consists of a smooth hard crust (paved sediment) mostly resulting from drying and aeolian erosion of paleo-sediments that is analyzed in detail in a companion paper (González-Romero et al., in prep.). ~~Dust is emitted frequently from here in favourable emission conditions~~ Under favorable weather conditions, dust is frequently emitted from this source area (González-Flórez et al., 2022). PSDs of the paved sediment were analyzed using dry dispersion (minimally dispersed) and wet dispersion (fully dispersed) techniques and displayed two prominent modes at $\sim$ 100 μm and $\sim$ 10 μm (González-Romero et al., in prep.). According to the fully dispersed PSD, the texture of the surface paved sediment is loam (Valentin and Bresson, 1992).

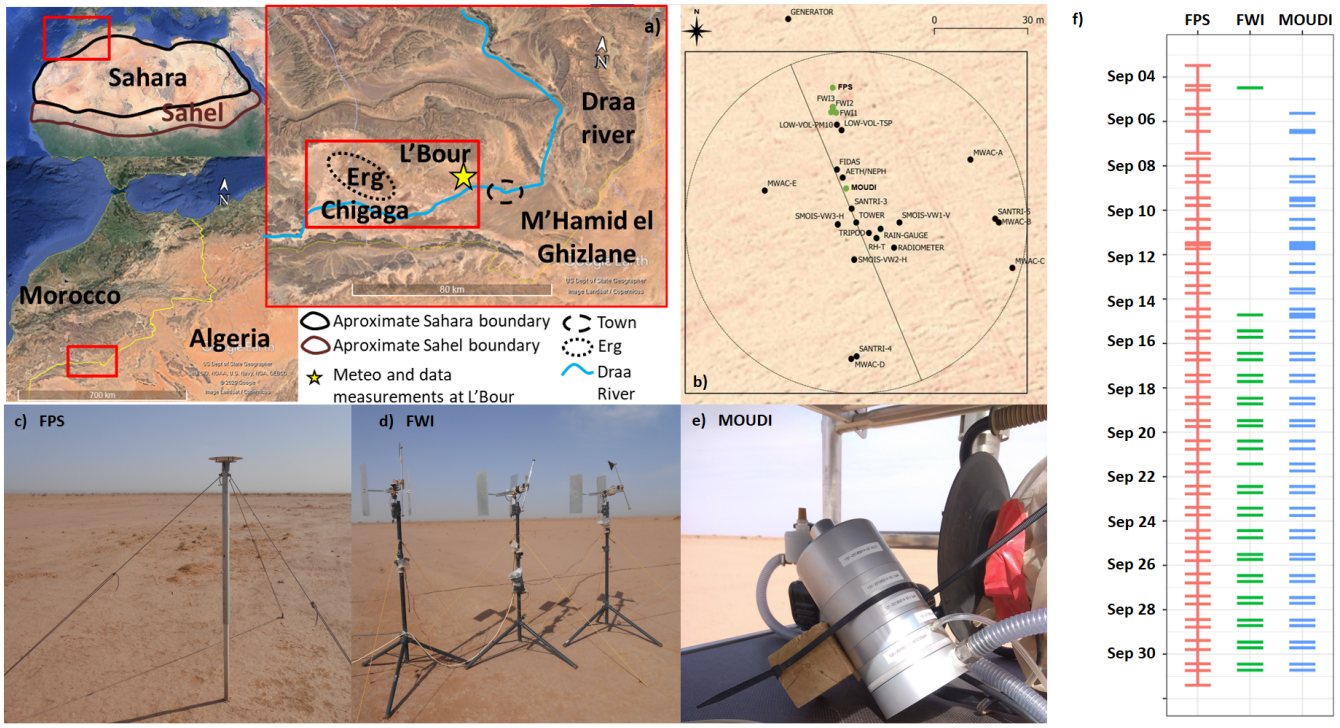

Figure 1. (a) Northwestern Africa showing area of operation of FRAGMENT campaign. The main location L'Bour is shown by a star sign which is located close to the Drâa river basin. (b) Schematic representation of different instruments used in the campaign with green dots highlighting those instruments used for single particle analysis. (c) Flat-plate deposition sampler (FPS). (d) Free-wing impactor (FWI). (e) Cascade impactor (MOUDI). (f) Sampling schedule of particle collection using different techniques. The horizontal bar represents start and end of sampling time. Note that due to very short sampling time for FWI and MOUDI, the two bars (start and end) appear as one. Image (a) was created using Google Earth (US Dept of State Geographer, Data SIO, NOAA, US Navy, NGA, GEBCO, ©2020 Google, Image Landsat/ Copernicus).

2.2 Sampling techniques

Particles were collected near ground level ($\sim$ 1.5 m) using three different sampling techniques, namely: flat-plate sampler (FPS), free-wing impactor (FWI), and a micro-orifice uniform deposit impactor (MOUDI, MSP Corp. Model 110) all of which are briefly described in the section below. A detailed description and methodology of sampling techniques have been provided in previous publications (Kandler et al., 2018; Waza et al., 2019). All aerosol samples were collected on pure carbon adhesive substrates (Spectro Tabs, Plano GmbH, Wetzlar, Germany) mounted on standard SEM aluminum stubs. Pure carbon substrate was chosen because of its excellent smooth surface resulting in a clear image-analytical separation of particles and background (Ebert et al., 1997). All adhesive samples were stored in standard SEM storage boxes (Ted Pella Inc., Redding, CA, USA) in dry conditions at room temperature. Substrates in the MOUDI and FWI were collected ~~two times a day~~ twice daily with a typical sampling duration of a few minutes to avoid overloading the substrate for individual particle analysis. For the flat-plate sampler, the average exposure time was half a day.

2.2.1 Free-wing Impactor (FWI)

A free-rotating wing impactor (Kandler et al., 2009, 2018; Waza et al., 2019) was used to collect particles larger than $\sim$3 μm (projected diameter). The FWI has a sticky carbon substrate as impaction surface as is attached to a rotating arm that moves through the air; particles deposit on the moving plate due to their inertia. The rotating arm is moved at a constant speed by a stepper motor, which is fixed on a wind vane, aligning the FWI to the wind direction. The substrate itself is oriented perpendicular to the air stream vector (resulting from wind and rotation speeds) by a small wind vane attached to the rotating arm. The particle size cutoff is ~~defined~~ determined by the impaction parameter, i.e., by rotation speed, wind speed, and sample substrate geometry.

2.2.2 Flat plate sampler (FPS)

The flat-plate sampler used in this work is based on the original flat-plate sampler used in Ott and Peters (2008). It consists of two round brass plates (top-plate diameter of 203 mm, bottom plate 127 mm, thickness 1 mm each) mounted with a distance of 16 mm separating them. The plates protect the substrate from precipitation and reduce the effects of wind speed by reducing the smallest turbulences to the distance between the parallel plates. In this setup, larger particles ($>$ 1 mm) cannot enter the sampling stub surface at low wind speed (Ott and Peters, 2008). The main ~~triggers~~ controls for particle deposition on the substrate are diffusion, gravity settling, and turbulent inertial forces.

2.2.3 Cascade impactor (MOUDI)

Sampling was conducted using a 5-stage Micro-Orifice Uniform Deposit Impactor (MOUDI, MSP Corp., MN, USA) with a 100 L min^{-1} flow rate. The impactor has stages available with 50% cut-point aerodynamic diameter (D_a) of 10, 2.5, 1.0, and 0.25 μm. Particles were collected on 25-mm sticky carbon substrates attached to the 75-mm impaction plate using a double-sided adhesive. The sampling time was chosen to provide optimum particle loading for single particle analysis which was

usually limited to a few minutes. The short sampling time resulted in fewer particle collections in the first two stages and therefore only the third and fourth stages ~~are chosen~~ were selected for detailed analysis.

Particle bounce can be an issue with an inertial impactor such as the MOUDI and occurs when particles ~~are impacted~~ impact on the collection substrate but are not retained. Studies have shown that particle bounce reduces at the relative humidity of $>$ 70 % depending on the ~~chemical composition~~ mineralogical properties of particles (Bateman et al., 2014; Fang et al., 1991; Vasiliou et al., 1999). During the measurement campaign, the relative humidity was usually below 60 % with a maximum of 71 % (see A1). Therefore, particle bounce can occur which could lead to biases in the particles collected. Additionally, the shattering and asphericity of dust particles can further induce bias in collected particles.

2.3 Scanning electron microscopy (SEM)

Size, morphology, and elemental composition of a large number of individual particles were investigated by SEM as done in previous studies ~~such as (Kandler et al., 2007; Chou et al., 2008; Ryder et al., 2018; Kandler et al., 2020)~~(Kandler et al., 2007; Chou et al., . About 64,000 (FWI), 100,000 (FPS), and 176,000 (MOUDI) individual particles were analyzed with a scanning electron microscope (FEI ESEM Quanta 400 FEG instrument, Eindhoven, The Netherlands) equipped with an X-Max 150 Energy-Dispersive X-ray spectroscopy (EDX) silicon drift X-ray detector (Oxford, Oxfordshire, UK) ~~. The~~ controlled by an AZtec 4.4 Oxford software. The AztecFeature software expansion was used to obtain particle data from thousands of particles in an efficient way. All of the samples were analyzed in high vacuum conditions without any pretreatment~~and were automatically detected using computer-controlled SEM with EDX (Oxford software AZtec 4.4)~~. Backscattered electron (BSE) ~~image~~ imagery was used for particle ~~identification~~ detection, as dust particles are composed of elements with atomic numbers greater than carbon and therefore visible as detectable bright spots in the BSE image. An acceleration voltage of 12.5 kV, beam current of 18 nA, "spot size 5.0" (beam diameter of $\sim$ 3 nm), and a working distance of approximately 10 mm were used to produce the optimum number of input counts ~~in~~ by the EDX detector. The scanning resolution was tuned to particle size. For ~~the~~ MOUDI and FPS, 160 nm per pixel was used to identify particles ~~up to~~ with minimum size of 0.5 μm projected area diameter ~~depending on the sample and for the~~ and for FWI, 360 nm per pixel was used to identify ~~the largest particles (mainly particles~~ particles larger than 2.5 μm in projected area diameter~~)~~. Chemistry information is derived by EDX. The internal ZAF correction (Z – atomic number, A – absorption, F – fluorescence, accounting for ~~material-dependent~~ matrix-dependent efficiencies) of the detector/-software system–based on inter-peak background radiation absorption measurements for correction–was used for obtaining quantitative results. The SEM-EDX ~~analysis normalizes the elemental composition~~ results are normalized to 100 %~~among the selected elements (~~, including those of the elements C, N, O, Na, Mg, Al, Si, P, S, Cl, K, Ca, Ti, V, Cr, Mn, Fe, F, Zn, and Pb~~)~~. The detection limits of each element are determined based on 2σ of the peak intensity and calculated with the AZtec software. A final sorting step is done to remove particles with low X-ray counts due to shading effects.

2.4 Particle morphology determination

2.4.1 Projected-area and volume-equivalent diameters

In the present study, the image analysis integrated into the SEM-EDX software AZtec is used to determine the size of particles as a projected area diameter. Projected area diameter, d_p, is the diameter of a circle having the same area as the dust particle projected in a two-dimensional image and is calculated as:

$$d_p = \sqrt{\frac{4 \times A}{\pi}}, \tag{1}$$

where A is the area covered by the particle on the sample substrate.

Following Ott and Peters (2008), the volume-equivalent diameter (sphere with the same volume as an irregular shaped particle) also called the geometric diameter, d_v, is estimated from the projected area diameter via volumetric shape factor expressed by particle projected area and perimeter (P) as follows:

$$d_v = \frac{4\pi A}{P^2} d_p = \frac{1}{P^2}\sqrt{64\pi A^3}. \tag{2}$$

All particle diameters (d) presented here are converted from projected area-equivalent diameter to volume-equivalent (geometric) diameter (unless stated otherwise). The reason for this conversion is that geometric diameter is used in global aerosol models to quantify dust size (Mahowald et al., 2014) and optical properties depend on the particle volume.

2.4.2 Aspect Ratio

The two-dimensional (2D) shape of individual dust particles is presented here as aspect ratio (AR) and was calculated by the image analysis integrated into the SEM-EDX software AZtec. AZtec software manual defines AR as the ratio of the major to the minor axis of the elliptical fit on the projected particle area. Symmetrical features, such as spheres or cubes, have an AR that is approximately 1 whereas features that have shapes like ovals or needles have an AR that is greater than 1. A critical shortcoming of 2-D imaging is that it can yield different shapes of 3-D particles depending on their orientations on the sampling substrate (Huang et al., 2020).

2.5 Number deposition rate calculation

The number deposition rate (NDR) is calculated from deposited particle numbers per area and individual particle size. First, a window correction (c_w) was applied (Kandler et al., 2009) to the particle deposition rate as

$$c_w = \frac{w_x w_y}{(w_x - d_p)(w_y - d_p)}, \tag{3}$$

where w_x and w_y are the dimensions of the analysis rectangle.

The NDR is then calculated as

$$NDR = \frac{1}{A \times t} \sum_i c_w(d_v, i), \tag{4}$$

where A is the total analyzed area, t is the sample collection time, and i is the index of the particle.

2.5.1 Determining the size distributions from free-wing impactor measurements

Obtaining the atmospheric ~~size distribution~~ PSD from FWI requires consideration of window correction and the collection efficiency dependence on the impaction speed and geometry. These corrections are applied to every individual particle as a function of its size and composition to get the overall collection efficiency (c_e) (for detailed formalism, see ~~S2~~section S3 of the Supplement). The atmospheric concentration (C) is then computed from the deposition rate and velocity as

$$C = \frac{1}{A \times v \times t} \sum_i c_w(d_v, i) c_e, \tag{5}$$

where A is the total analyzed area, v is the impaction velocity, t is the sample collection time, and i is the index of the particle.

2.5.2 Determining the size distributions from the flat-plate sampler and cascade impactor measurements

Obtaining atmospheric concentrations from the NDR requires the use of different deposition velocity models for the flat-plate sampler. There exist a variety of models to estimate particle deposition speed based on a set of assumptions and neglections (Noll et al., 2001; Aluko and Noll, 2006; Piskunov, 2009; Petroff and Zhang, 2010). However, non of these models fitted the observed deposition velocities, which appeared to be rather uniform in Waza et al. (2019). Therefore, for the present work, a constant deposition velocity for the size range of interest was assumed and the ~~size distributions were normalized and averaged over all measurements~~ PSD were normalized by fitting the number (N) size distribution to the power law $dN/d\log D_p = cD_p^{-2}$, and dividing all measurements by the fitted proportionality constant c (Kok, 2011). For the MOUDI samples, atmospheric concentrations cannot be determined with the analytic approach used in this work because the size of the impaction spot cannot be retrieved with high accuracy to get the total number of particles deposited at each spot. Therefore the same approach as FPS is applied to the MOUDI samples to get the ~~size distribution~~PSD. In addition, direct comparison is often difficult among different instruments due to the different nature of particle collection from each technique (Chou et al., 2008; Price et al., 2018).

2.6 Particle classification and composition

SEM-EDX ~~detects~~ measures the elemental composition of individual dust particles. Some minerals have well-defined compositions and can therefore be ~~identified relatively easy~~ readily identified (e.g. gypsum, quartz, calcite). Others, e.g. clay minerals, are variable in nature, so their identification is more ambiguous. Moreover, dust particles are commonly found in the form of internal mixtures or aggregates rather than in their pure mineral forms, and therefore the method used in this study identifies the

major mineral type in each particle. As there is no standardization that is suitable for characterization of mineral dust aerosols using SEM, different approaches have been developed ranging from a simple scheme (Kandler et al., 2007, 2009) to more complex ones (Kandler et al., 2011, 2018). In comparing different desert aerosols (Kandler et al., 2020), plausible differences related to geology and weathering conditions were observed, but in particular between different techniques (Marsden et al., 2019) there will remain biases.

Particle classification in this study is supported by the analysis of dust and soil samples for the major mineral composition from X-ray diffraction (XRD) measurements reported in a companion paper (González-Romero et al., in prep.). Furthermore, to assess artefacts, a few clean blank samples taken during the campaign were scanned and certain particle types could be identified as contaminants and thus discarded from the analysis. The contaminants detected consisted of pure iron (apparently already from the manufacturing process) and F+Si. The contaminants were mostly rare compared to the abundance of dust particles.

Based on the single particle composition quantification, an elemental index for the element X is defined as the atomic ratio of the concentration of the element considered and the sum of the concentrations of the elements quantified (Kandler et al., 2007, 2018)

$$|X| = \frac{X}{Na + Mg + Al + Si + P + S + Cl + K + Ca + Ti + Cr + Mn + Fe + Co}, \tag{6}$$

where the element symbols represent the relative contribution in atom % measured for each particle. Note that the given method ~~cannot be used~~ was not applied to quantify the percentage of C, N, and O due to their high uncertainty and substrate contributions. ~~Classification is~~ The method used to analyze particles collected on substrates follows our previous work (Kandler et al., 2018) and therefore the approach is only described briefly here. Classification was done using a set of rules, which use the elemental index and additional elemental ratios and are defined by the dominance of one or more specific elements or their ratios (e.g. Al, Si, Ca, Fe, Al/Si). Particle classes are named for their most prevalent chemical component(s), which may contain terms for mineral phases to simplify the naming (e.g. gypsum, quartz). ~~Those mineral phases were chosen as the most prevalent components that matched the reported elemental composition, but no real~~ The mineral labels were assigned from the best match to the measured elemental concentrations. There was no actual phase identification of individual particles (e.g., by transmission electron microscopy) was carried out. Therefore, all the particle classes are termed '-like' to express the similarity in chemical fingerprints. Details of the classification procedure are given in section S1 of the Supplement.

2.7 Ancillary data

Aerosol PSDs of suspended mineral dust were also obtained by using an Optical Particle Counter (OPC, FIDAS 200, Palas GmbH, Germany). The measurement range of FIDAS was 0.2 - 19 μm with a time resolution of 2 min and a flow of 4.80 L min^{-1}. Data acquisition was performed by a data logger, averaging measurements over 2 min. In addition, meteorological data were acquired with a time resolution of 1 s. Air temperature and relative humidity were measured by HC2A-S3 sensor (Campbell Scientific) and wind speed, and wind direction was recorded by a two-dimensional sonic anemometer (Campbell

Scientific WINDSONIC4-L) during the sampling period at approximately 0.4 m, 0.8 m, 2 m, 5 m and 10 m height facing north above ground level (see Fig. ~~??~~A1). The average OPC concentration PSD is used here for comparison purposes. ~~In~~ The default optical diameters were transformed into dust geometric diameters assuming dust asphericity and aspect ratios obtained with SEM aspherical dust. The details are described in a companion paper (González-Flórez et al., 2022) ~~, the emitted~~ that thoroughly analyzes the emitted flux PSD and its variability~~are analyzed in detail~~.

2.8 Statistical analysis

The uncertainty in the counting statistics for various particle groups was determined by generating confidence intervals assuming binomial distribution, i.e. for a relative number abundance of a particular particle group *r*, the two-sided 95 % confidence interval is approximated (Hartung et al., 2012). ~~For the obtained PSDs, the only error source considered is the Poisson counting error.~~

3 Results and discussion

3.1 Observed particle types

Typical chemical compositions of a set of minerals and boundary rules were used to define particle groups (see section S1 in the Supplement). Based on ~~the applied scheme~~set classification rules, particles were assigned to ~~the following classes: (i) oxides/hydroxides, (ii) feldspar, (iii) clay minerals, (iv) quartz-like and complex quartz-like, (v) other silicates (vi) Ca-rich, (vii) sulfates, and (viii) mixtures and others~~different types. Each of these particle types is discussed further in section S2 of the Supplement. Figure 2 ~~shows the~~ and Table S2 in the Supplement show the average elemental composition of these groups. However, it is important to ~~note that~~ treat this classification scheme with caution as each particle can be composed of different minerals~~and~~ , which in part can have variable ~~and even indistinguishable compositions. Therefore, the created groups may not only consist of the minerals described below.~~ or ambiguous compositions. As a result the groups used do not uniquely identify a mineral, but instead show the most probable mineral matching a particle composition. This is reflected in the suffix -like used in the group nomenclature. As there are other potential identification approaches, with their own associated advantages and limitations, the full data set generated and used in this study is provided for future studies.

3.1.1 ~~Oxides/Hydroxides~~

~~This class consists of hematite-like and anatase-like particles with Fe and Ti X-ray signals dominating, respectively. Both particle types were mainly found in particles with $d_v < 2.5$ μm with anatase-like particles being rare. Iron (Fe) oxides are present both in pure crystalline form and as small impurities attached to other minerals. Moreover, Fe is present in other particle groups as well, mainly in clays and silicates. However, the presence of Fe can be due to not only Fe oxi(hydroxi)des but also to structural Fe. Fe oxides tend to exist as separate individual particles in sizes $d_v < 2$ μm and with increasing aggregate~~

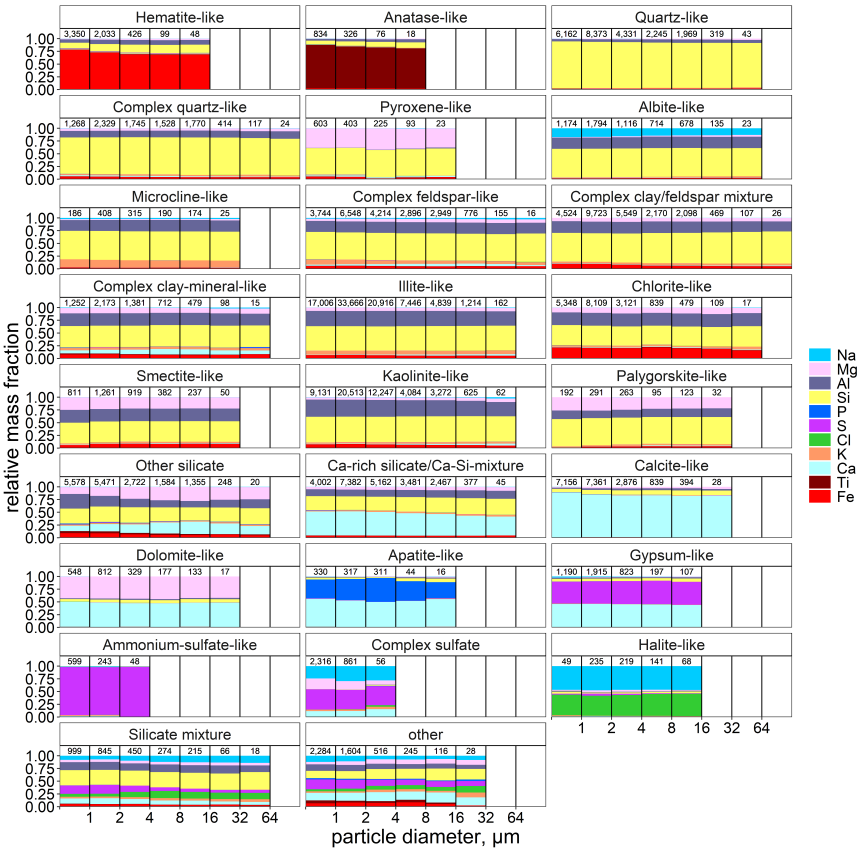

Figure 2. Average elemental composition as a function of particle size for different particle groups. The legend shows element index for each respective element. The numbers on top represent total particle counts in the given size bin. Abundance bars are not shown for size bins with fewer than 10 particles.

~~size could be distributed as small grains throughout the aggregate volume. The number abundance of this class was usually below 2 % in the collected samples.~~

3.1.1 ~~Quartz-like and complex quartz-like~~

~~The classification of particles into quartz-like is relatively straightforward with a dominant Si signal. Some of the particles with high Si were also found with slightly higher Al content associated with them and are therefore classified as complex quartz-like. Fe content is generally low, suggesting that Fe oxides are not linked with quartz-like particles. The particle number abundance of quartz-like particles was ~ 8 % and complex quartz-like particles ranged from 1 % to 15 % depending on particle size.~~

3.1.1 Feldspar-like and pure feldspar abundance

The feldspar group is characterized by Si:Al:K / Si:Al:Na signal ratios of approximately 3:1:1 for microcline-like (K-feldspar) and albite-like (Na-feldspar), respectively. Ca-feldspar-like particles are quite rare in the samples. Na-feldspar particles are present across all size ranges ranging from 1.5 % in particles with $d_v < 2.5$ μm to around 3 % in particles with $d_v > 2.5$ μm. K-feldspar particles on the contrary are present in <1 % and are found mainly in particles with $d_v < 5$ μm. The complex feldspar-like and complex clay/feldspar mixture have Si:Al signal ratios of approximately 3:1 with additional elements such as Ca, Fe and Mg, suggesting a more complex aggregate than a pure feldspar. Complex feldspar-like particles were found in the range of 5 - 8 % in particles with $d_v < 20$ μm. For particles with $d_v > 20$ μm , its occurrence was about 15 %. Similar number abundances were also observed for complex clay/feldspar mixtures.

Regarding the identification of feldspars, there are two approaches: One is based on the classical 'classification' scheme, where a fixed limit around the usual composition of feldspars is used (detailed formalism in S1), and the other is the feldspar-specific index approach, where a distance from the ideal composition is calculated. Both form different shapes in the x-dimensional element space and therefore lead to different results. The index approach has the advantage that it shows how close a particle is to an ideal composition. In this case, the feldspar indices regard the overall contribution of feldspar-specific elements to the particle and the specific Al/Si as well as alkali/Si or K/Si ratios. It was found that an index value of > 0.80 is suitable to distinguish between pure feldspar grains and other silicates. Details of the index calculation are given in S3.

3.1.1 Ca-rich

Calcium-rich particles include calcite-like, apatite-like, dolomite-like, and gypsum-like and these are characterized by high Ca, Ca+P, Ca+Mg, and Ca+S content, respectively. In gypsum-like the Ca:S weight ratio is $\sim$ 1 and in dolomite-like particles the Ca:Mg weight ratio is $\sim$ 1. Apatite-like particles were quite rare and only present in a few samples. The majority of the particles were calcite-like and their abundance was usually around 8 % in the collected samples, with a higher proportion in $d_v < 5$ μm. This group did not include particles with appreciable Fe contents in contrast to other classes (Fig. 2).

3.1.1 Clay minerals

Clay minerals can be divided into four subgroups: kaolinite-like, illite-like, smectite-like, and chlorite-like, with illite and kaolinite having a similar average Si-to-Al signal ratio (1.6 and 1.5 respectively) , but with illite-like containing K, Fe and Mg whereas in kaolinite-like particles K is present in trace amount. These are the most abundant particle types found in the collected sample with number abundances of 25 % and 15 %, respectively. Smectite-like particles are clay minerals containing Fe and Mg, as well as small amounts of Ca and are found across all size ranges in small proportions (< 1 %). Chlorite-like particles are characterized by slightly higher Fe content compared to other clay minerals and their relative contribution is around 5 % in particles with $d_v < 5$ μm and 2 % in particles with $d_v > 5$ μm.

3.1.1 Other silicates

The other silicate class group are characterized by the presence of Si and Al together with trace amounts of Mg, Ca, and Fe. Another silicate group in this class are Ca-rich silicates/Ca-Si-mixtures. These are typically clay minerals particles that are internally mixed with Ca carbonates (e.g. calcite). Furthermore, Fe is also a minor component in this particle class suggesting an additional contribution of Fe oxides. The particle number abundance of other silicates class is $\sim$ 5 % and that of Ca-Si mixtures varies between 5 % to 12 % depending on particle size.

3.1.1 Sulfates

In the sulfate group, mainly ammonium sulfate-like particles were present (i.e. only S was detected in a particle). They make up a very small amount in the total sample ($<$ 0.25 %) as individual particles and are mostly observed in particles with $d_v > 2$ μm. Ammonium sulfate is the prevalent sulfate species present in atmospheric aerosols and it has an anthropogenic secondary origin.

3.1.1 Mixtures and other

The silicate mixture group are dominated by Si along with the presence of other elements in varying amount and therefore does not belong to any other defined silicate group. The so-called 'other' group contains all particles that are not classified by the applied scheme into any of the groups described above. Therefore, it represents a mixture of different minerals or rare species. The relative number abundance for mixtures was around 4 % in the collected sample and the number percentage of the 'other' group is substantially low ($<$ 0.5 %).

3.1.1 Silicate composition

The dominating composition in mineral dust is silicates which are composed of different minerals. Figure **??** shows the highly variable chemical composition of the silicate particles with (Mg+Fe)/Si ratio (x-axis), Al/Si ratio (y-axis), and the (Na+K+Ca)/Si ratio (z-axis, colour-coded) for each single particle.The three main clusters visible in Fig. **??** are numbered 1 (quartz-like), 2 (feldspar), and 3 (most other particles). Like mentioned in Kandler et al. (2011), the Al/Si ratio exhibits the least measurement uncertainty and varies significantly for different minerals. The (Mg+Fe)/Si ratio is an indicator for clay mineral aggregates as feldspar does not usually contain these elements (Anthony et al., 2003). The (Na+K+Ca)/Si ratio can be used to differentiate between feldspar and clay minerals as feldspar shows much higher values as compared to clay minerals. However, it can be also seen that this distinction is usually not clear-cut as all dust particles are usually 'contaminated' with other minerals and the aggregates have ambiguous compositions.

Scatter-plot for silicate particle composition. The three main clusters are marked by numbers: (1) quartz cluster, (2) feldspar cluster, and (3) clay mineral/aggregate cluster.

3.2 Comparison of PSD of different techniques for particle collection

~~Figure 3 (a) shows the normalized number size distributions obtained by FPS, MOUDI, and OPC. The size distribution obtained by FPS~~ Figure 3 (a) presents normalized PSD obtained by FPS, MOUDI, and OPC as described in section 2.5.2. The normalization allows to easily compare the shape of the PSD obtained with the different techniques, i.e, the relative contribution of particles of different sizes. The PSD obtained by the FPS shows good agreement with that obtained from the OPC. The ~~size distribution of~~ PSD of the measured volume equivalent diameter is towards the higher end of the cut-off aerodynamic diameter expected on individual MOUDI stages. In stage 3, the mode is at around 3 μm (nominal cut point 2.5 μm) and for stage 4 the mode is at 1 μm (nominal cut point 1 μm). Figure 3 (b) shows the ~~number size distribution obtained by~~ PSD obtained by the FWI and is compared with the ~~atmospheric size distribution~~ PSD from the OPC. A clear discrepancy is observed between FWI and OPC ~~which~~ that is larger than the statistical uncertainties. Here, the FWI substantially underestimates particles < 10 μm. The collection efficiency of the FWI is 50 % for 11 μm aerodynamic diameter particles (Kandler et al., 2018) and therefore for fine mode particles the efficiency correction function can result in unrealistic values. For ~~diameter~~ diameters > 10 μm, the shape of the ~~size distribution~~ PSD is similar to that of the OPC but the observed concentrations are still an order of magnitude smaller. The discrepancy may be linked to one or more of the following potential sources of uncertainty: ~~a badly~~ not well defined efficiency curve for ~~FWI, the discrepancy in particle size definition (optical measured diameter versus projected area equivalent diameter)~~ the FWI, and particle density estimation from SEM to calculate volume equivalent diameter for efficiency correction. ~~As~~ In this contribution, the shape (and not absolute concentrations) of the ~~number size distribution is~~ PSD is relevant and is quite similar among the different measurement techniques used and OPC~~and~~ . It therefore provides confidence in the derived size-resolved elemental composition by SEM.

3.3 Particle composition

~~Figure 4 shows the time-averaged composition of the aerosol at L'Bour from~~ The dependence of composition on size is shown in Fig. 4 and Table **??** for aerosol samples collected with ~~the~~ three different sampling techniques. Since the composition of the aerosol particles in each sample does not exhibit a large sample-to-sample variability (see Fig. ~~S1,~~ S2, S3, S4 for individual samples), all of the dust sample compositions were merged for further comparison. ~~Relative number abundances are given in terms of particle group.~~ Furthermore, as the collection efficiency by size is less relevant to the fractional contribution of each mineral type per size and therefore integrating all the techniques together improves the statistics per each size with higher number of particles analysed.

A clear trend is seen among the different particle groups based on their size. Clay minerals are the most abundant and are present across all size ranges. ~~Similarly, quartz-like~~ Quartz-like particles are found in each size class with almost similar ~~number~~ mass abundance (around ~~6~~ 5-8 %) whereas the ~~number~~ mass fraction for complex quartz-like grows with particle size from 2 % in $d_v < 1$ μm to 22% in $d_v > 64$ μm. This suggests that as particle size increases, quartz particles get internally mixed with elements like Al and Fe forming complex aggregates. ~~A~~ Likewise, a similar trend is ~~also~~ observed for feldspar particles where complex feldspar-like particles increase with particle size as a result of the inclusion of other elements creating a complex mixture. This observation is consistent with Engelbrecht et al. (2016, 2017) that found larger particles to be generally present as aggregates and coatings on other mineral particles. A detailed discussion on feldspar particles is addressed further in

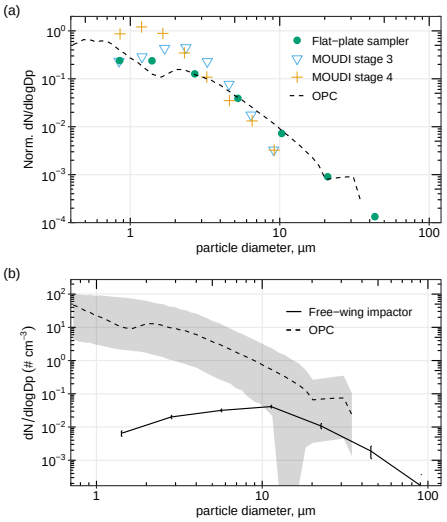

Figure 3. (a) Normalized ~~number~~ particle size distribution obtained by different sampling techniques averaged over the entire campaign period. (b) Comparing the atmospheric ~~number~~ particle size distribution between FWI and OPC. The bold line is for FWI with error bar showing the Poisson counting error and dashed line indicates the field campaign mean size distribution from OPC and the shaded region shows the 95th and 5th percentile. Note that below $\sim$ 15 μm diameter, the collection efficiency of the FWI drops significantly.

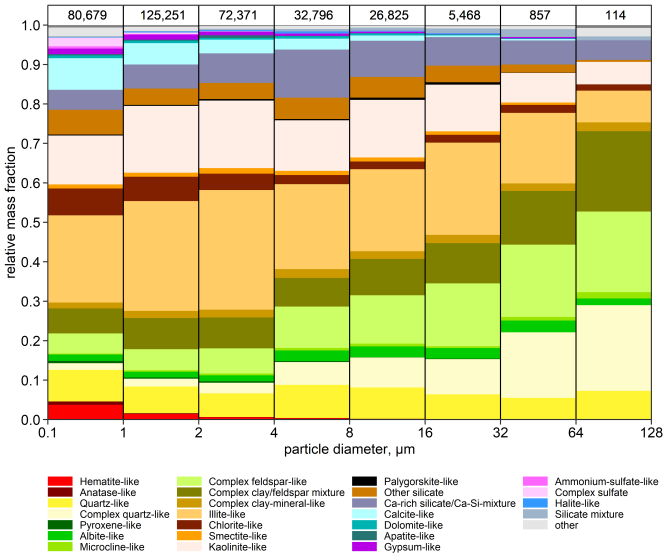

Figure 4. Average size-resolved mass abundance of different particle groups. The numbers on top represent total particle counts in the given size bin.

Sect. 3.3.4. ~~Furthermore, the~~ Fe-rich particles are present in low quantities and decrease with particle size. As they are highly relevant in controlling spectral shortwave refractive index (Engelbrecht et al., 2016; Caponi et al., 2017; Di Biagio et al., 2019) , they are further discussed in detail in section 3.3.3. Furthermore, iron is detected across the all the size classes and present in most of the particle groups. This could further have implications for the absorption as absorption increases with particle size which could be further enhanced because of the iron content. Similarly, the proportion of Ca-rich ~~, Fe-rich, and sulfate-like particles tends to decrease with increasing size~~particles (calcite, dolomite as well as gypsum and apatite) are mainly confined to particles smaller than 4 μm. The Ca-Si mixture is slightly enhanced at $d_v > 4$ μm which could be due to the availability of more silicates to form aggregates with calcite and also the depletion of illite-like particles could partly form aggregates with calcite too.

~~On average across all particle sizes, 26 % of particles are illite-like, 14 % kaolinite-like, 10 % quartz and complex quartz-like, 7 % complex clay/feldspar mixture, 6 % Ca-rich silicate/Ca-silicate mixture, 5 % chlorite-like, 5 % calcite-like, 1.7 % hematite-like, 1.7 % albite-like, 1.3 % gypsum-like, and 1.2 % smectite-like. The contribution of ammonium sulfate particles is restricted to particles with d_v~~ Sulfate-like particles are mainly present in the smallest size bin of $<$ ~~2.5~~ 1 μm. ~~Chamber studies of Moroccan soil have shown a dominance of illite-smectite clay minerals in the size $<$ 2.5 μm (Marsden et al., 2019). Our observed composition is fairly similar to the chemical composition~~ These are most probably anthropogenic/secondary aerosol as corroborated with measurements of optical properties (Yus-Díez et al., in prep.) and PSD (González-Flórez et al., 2022).

Studies on individual particle analysis of mineral dust by SEM/EDX have provided insights into the compositional variability, size and morphological characteristics of dust particles from different regions. Kandler et al. (2009) presents composition of Saharan mineral dust collected during the SAMUM campaign from in situ measurements at Tinfou, Morocco in May/June 2006 ~~(Kandler et al., 2009). However, a detailed comparison is not possible due to the inadequately subdivided silicates classes in Kandler et al. (2009). Moreover, the observed composition type is corroborated with XRD analyses of particle size fractions separated from the sediments of L'Bour during the same sampling campaign (González-Romero et al., in prep.). Furthermore, samples from Morocco (Kandler et al., 2009) and transported Saharan dust at Tenerife (Alastuey et al., 2005) also showed similar composition from XRD analysis. Additionally, Kandler et al. (2009, 2011) found the fraction of quartz-like particles to increase with particle size~~ and thus providing an ideal comparison to our findings. On average, their particle composition between 0.5 μm and 50 μm diameter is also primarily alumino-silicates with a smaller contribution of quartz and calcium-rich particles. However, one finding of note from Kandler et al. (2009) is the observation of quartz fraction to increase with particle size, mainly for particles larger than 20 μm in diameter. Although our result reveal the quartz/complex-quartz-like to increases with particle size, it is not the dominant component as reported in Kandler et al. (2009). Marsden et al. (2019) present the mineralogy and mixing state of particles smaller than 2.5 μm in laboratory-suspended northern African dust using SEM. They found a dominance of clay minerals in the size $<$ 2.5 μm which is similar to the observations reported in the current study. Scheuvens et al. (2011) observed compositional homogeneity of dust over southern Morocco, consistent with our results indicating dust at source regions to be not usually affected by anthropogenic components. Additionally, compositional and morphological homogeneity was also reported by Chou et al. (2008) for dust samples taken over Niger. Nevertheless, our study shows distinct compositional signatures of prominent source area (e.g. occurrence of apatite-like particles, elevated

Ca-rich content). For the middle east, Jish Prakash et al. (2016) reported relative mass abundance of 45-75 % clay minerals, 5–54 % feldspar, and 0.1–10.2 % quartz as main components, while calcite, dolomite, gypsum, and iron oxides were the minor constituents of individual dust particles in the size range 0.5–38 μm. This is quite similar to our results if the 'complex' part of the quartz and feldspar fraction together with its 'mineral-like' component is considered as one fraction suggesting a similarity between Arabian and Saharan dust. A separate study from Engelbrecht et al. (2009a) found quartz and feldspars to be dominant particle type in Kuwait while calcite and dolomite were major components in the dust particles from the UAE and Iraq. This is quite different to the mineralogy in our study and could be due to the different chemical weathering regime and the composition of the parent sediments. In Asia, Jeong (2008) reported mineralogical properties of Asian dust to mainly consist of clay aggregates (48 %), quartz (22 %), plagioclase (11 %), calcite (6 %), and K-feldspar (5%). The mineral composition of Asian dust therefore has a higher K-feldspar content compared to our findings in Morocco while illite is observed in both the Asian dust and our study as major clay mineral. ~~As dust originating from N Africa (Morocco, Algeria and Tunisia) can be subject to long-range transport (Engelstaedter et al., 2006; Müller et al., 2009), events like red rains over Montseny mountains in Spain (Avila et al., 1997) and south-eastern part of Italy (Blanco et al., 2003) have been reported . Mineralogical analysis of samples from the studies above detected quartz, clay minerals (illite > kaolinite), and carbonates (calcite > dolomite) in a greater proportion with feldsparand smectite as other major mineral components(Avila et al., 1997; Alastuey et al., 2005). Few elements can be considered as a source tracer; for example, high Ca content is usually associated to be a tracer for dust emitted from Morocco (Kandler et al., 2007) which is also found in our result by single particle analysis. Mineralogical database of soil composition also show high amounts of calcite and illite in north Sahara (Claquin et al., 1999) again corroborated by our single particle analysis.~~

~~Average size-resolved relative number abundance of different particle groups. The numbers on top represent total particle counts in the given size bin.~~

3.3.1 Particle abundances using different techniques

Figure 5 shows the compositional information for dust samples obtained using 3 different collection techniques. These techniques have different collection efficiencies, target size ranges, and sampling intervals. The goal was to get a representative number of particles across a wide size distribution, which is usually the case for mineral dust. However, the collection of particles larger than a few micrometres is relatively difficult due to the poor collection efficiency of many instruments. Therefore, in this work an inlet-free impactor i.e. FWI was used to sample particles with $d_v > 3$ μm whereas FPS and MOUDI were used primarily for particles having $d_v < 3$ μm. The non-parallel sampling time of the sampling techniques during the present field campaign could not be avoided as FWI and MOUDI operate actively while the FPS operates passively. The active samplers have a much higher collection velocity. This requires short sampling time for the two active samplers. On the contrary, the passive sampler (i.e., FPS) require a much longer sampling time. Using the same collection time would result in either underloading of the passive or overloading of the active samplers.

In the MOUDI sample, most of the collected particles (> 97%) had $d_v < 5$ μm. In stage 3 (cut-off d_a 1 - 2.5 μm), 56 % of the collected particles were within the specified stage size range; the size of half of the remaining particles was below

the lower cutoff and that of the other half was above the upper cutoff. The major constituents were illite-like, kaolinite-like, quartz-like, Ca-silicate mixture, complex clay/feldspar mixture, and calcite-like with feldspar-like, quartz-like, hematite-like and sulfates as minor constituents. A similar trend was also observed in stage 4 of MOUDI except for an enhanced abundance of kaolinite-like and complex clay particles. In the FPS samples, the number of collected particles in the size range $0.1 < d_v < 5$ μm is quite comparable to stage 3 of MOUDI. For particles with $d_v > 5$ μm, the composition changes only slightly by increasing quartz-like and decreasing calcite-like particles. In the FWI samples, more than 70 % of particles had $d_v > 5$ μm. The number abundance of feldspar-like, quartz-like, complex feldspar-like and complex clay/feldspar mixture particles increases with increasing particle size, while the number abundance of clay-like particles tends to decrease. In contrast, calcite-like, gypsum-like, and sulfates are virtually absent in samples from FWI in $d_v < 3$ μm which is the size range where they are typically observed. However, the number of particles analysed in the given size is significantly less compared to FPS or MOUDI. Note that it was not possible to perform sampling with FWI and MOUDI under the highest dust concentrations due to the high concentrations and as a consequence extremely short sampling times, which would have been necessary.

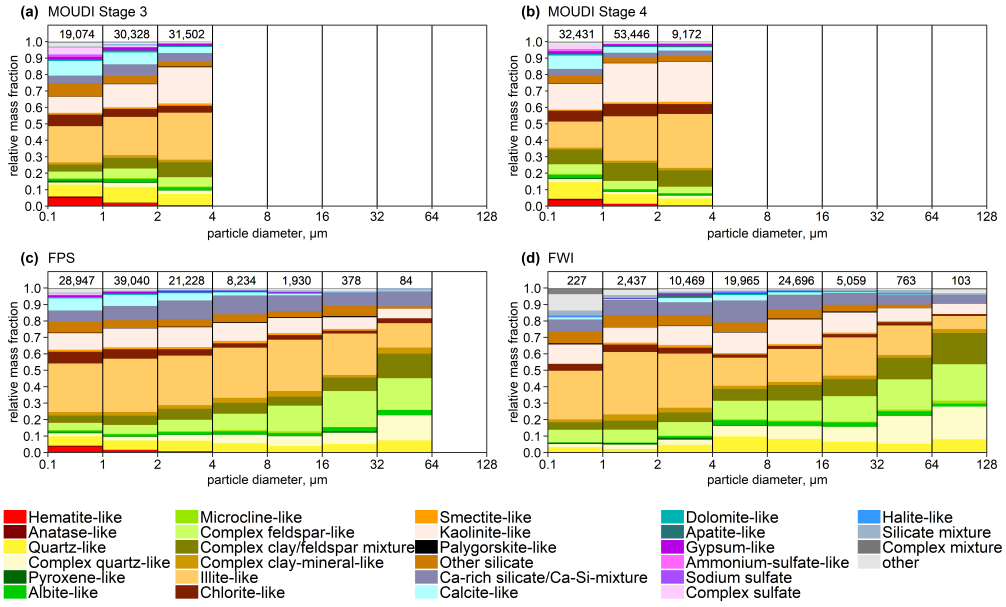

Figure 5. Average size-resolved mass abundance of different particle groups using different sampling techniques collected over the campaign period. The numbers on top represent total particle counts in the given size bin. Abundance bars are not shown for size bins with fewer than 30 particles.

Differences in abundance for some of the classes among the different techniques might be due to the way by which particles reach the substrate. In MOUDI and FWI, particles are impacted on the substrate whereas in FPS particles are deposited by gravitational settling and turbulent diffusion. One hypothesis for such difference is that in the MOUDI the high impaction speed experienced by particle aggregates on the top stages may break some of them into smaller ones and get carried away

along the ~~jet streams on the bottom~~ air streams onto the lower stages. Such a hypothesis is consistent with the enhancement of clay-like aggregates in MOUDI. Other observed differences between the sampling techniques could be related to the non-parallel sampling times. MOUDI and FWI samples represent a few minutes compared to the usually half-day exposure time for FPS. However, as variations in the composition are fairly similar for all of our analysed samples, the latter is most likely not a major aspect.

~~Average size-resolved relative number abundance of different particle groups using different sampling techniques collected over the campaign period. The numbers on top represent total particle counts in the given size bin. Abundance bars are not shown for size bins with fewer than 30 particles.~~

3.3.2 Temporal variability

Figure 6 displays time series of number abundances in three size ranges for the different particle groups observed in deposition samplers. While the dependence of ~~chemical composition on particle size~~ particle size distribution on sample mineralogy is quite strong, the temporal variation of the major particle groups does not show significant variability. This behaviour is to be expected as sampling was done in the source region, and the average daily composition is relatively constant.

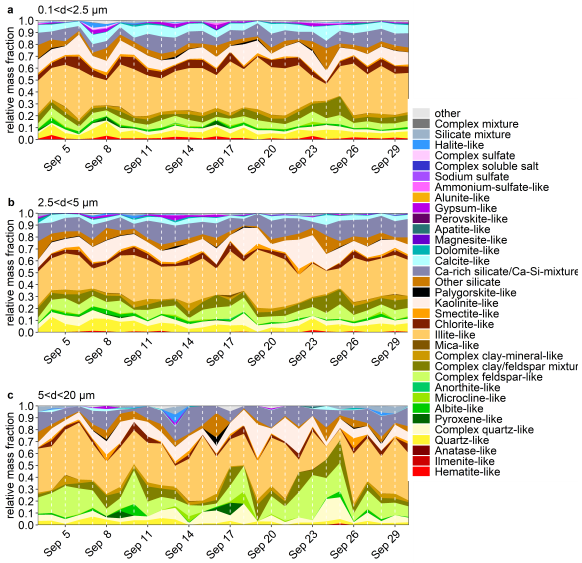

Figure 6. Time series of chemical composition for particles in (a) $0.1 < d < 2.5$ μm, (b) $2.5 < d < 5$ μm and (c) $5 < d < 20$ μm in L'Bour.

Nevertheless, looking at specific samples we can observe distinct compositional differences. Figure 7 shows chemical composition for four different situations. Secondary sulfates were dominant in particle $d_v < 2$ μm in samples collected during 8-10 September when the wind comes from the east (i.e. M'Hamid) suggesting anthropogenic origin which is further corroborated with measurements of optical properties (Yus-Díez et al., in prep.) and PSD (González-Flórez et al., 2022). This was also observed for small particles in the SAMUM campaign in Tinfou, Morocco (Kaaden et al., 2009). Apatite-like particles

were almost non-existent in our samples except for some specific days (20 and 23 September). ~~As potassium (K) peak was not observed, windblown fertilizer as a source can be discarded~~They were identified by the presence of Ca and P. Furthermore, ~~the particles were~~ manual inspection of the particles showed it to be not beam-sensitive ~~and~~ with no Cl and F signals ~~were detectedsuggesting~~ detected. Even though hydroxyapatite [$Ca_5OH(PO_4)_3$] is not commonly found in the Morocco phosphate deposits, the absence of Cl and F suggests it to be OH-apatite originating from a distinct geogenic source. Most of these particles were confined to size d_v 2-4 μm. In these particles, phosphorus is attached to the crystal lattice; ~~which~~ phosphorus is one of the important dust-derived nutrients for marine and terrestrial ecosystems controlling phytoplankton productivity and carbon uptake (Stockdale et al., 2016). The ~~solubility of these particles is not known but can be estimated to be low (Prospero et al., 1996). Therefore, the amount of phosphorus available as a nutrient for marine or terrestrial ecosystems in our sample is expected to be relatively low. The sampling day (~~sampling day of 24 September ~~)~~ is characterized by elevated Ca-rich particles making it the most calcium-rich day and were present mainly in $d_v < 1$ μm. Here it was present in 30 % compared to the average of 5 %. This observation could be due to advection from a prominent dust source. Furthermore, the iron-rich particle is also quite pronounced on this day indicating a special source imprint.

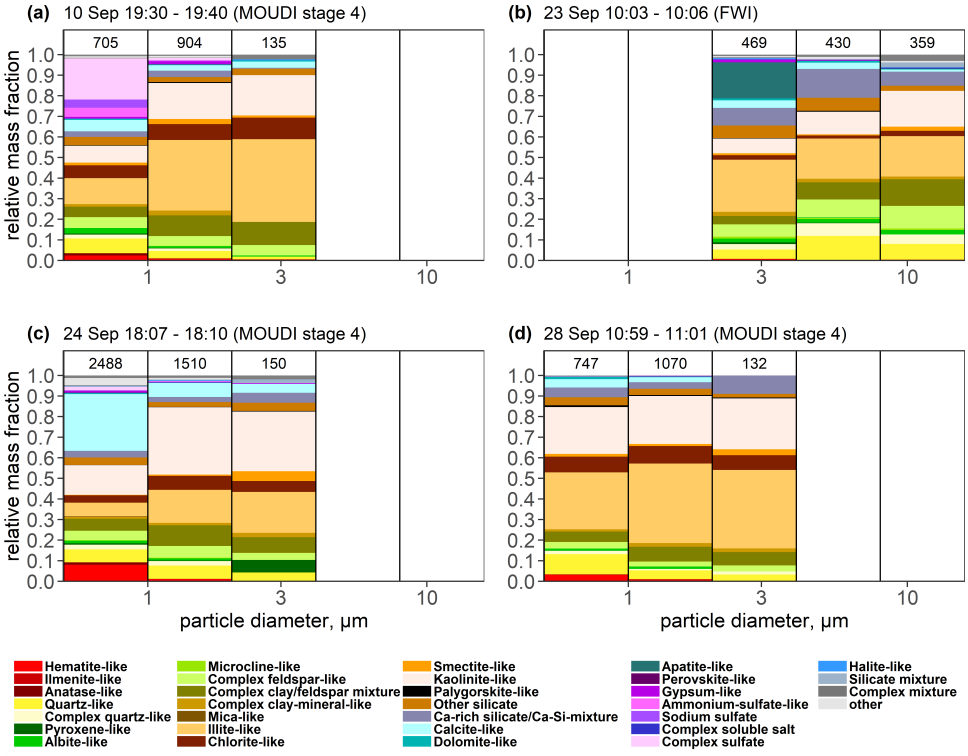

Figure 7. ~~Size distribution~~ Phase compositions of ~~the particle relative number abundance~~ size bins for ~~4 different situations~~samples collected under specific meteorological conditions at specific times and on certain days: (a) sulfate episode (b) apatite particle (c) Ca-rich episode and (d) typical average composition. The total number of analyzed particles ~~in~~ is given for each size class with fewer than 30 particles not shown.

3.3.3 Iron distribution

~~Many minerals such as feldspars, clays~~ Clay minerals and Fe-oxi/hydroxides such as hematite, goethite and magnetite, contain Fe, which is a key ingredient to numerous climatic, environmental and biological processes affected by dust (Schulz et al., 2012). Fe in minerals can be broadly classified into structural Fe, which is typically found in the crystal lattice of clay minerals, and Fe in the form of oxide or hydroxide particles (mainly hematite and goethite) (Kandler et al., 2009; Scheuvens et al., 2011). The amount of free Fe-oxi/hydroxides along with its size, and aggregation or mixing state (internal vs external mixing) with other minerals determine the degree of absorption of solar radiation by dust ~~(Sokolik and Toon, 1999; ?; Zhang et al., 2015; Di Biagio et al.~~ (Sokolik and Toon, 1999; Moosmüller et al., 2012; Zhang et al., 2015; Di Biagio et al., 2019), and the potential Fe solubility (Baker and Jickells, 2006; Marcotte et al., 2020) of the deposited dust that fertilizes the ocean. In addition, it has been suggested that ocean primary productivity depends not only on the dissolved Fe but also on suspended solid Fe particles and their mineralogical components (Hettiarachchi et al., 2021). Furthermore, dust absorptive properties vary in different source regions mainly due to variations in the Fe oxides fraction (Lafon et al., 2006). While SEM cannot distinguish between structural and free Fe, by providing the total Fe content on a particle-by-particle basis, it can provide some useful clues on the mixing state of Fe-oxi/hydroxides.

To understand the Fe content and to some extent the mixing state along with the type of particles that Fe is associated with, Fig. 8a shows the relative abundance of particles classified into nine categories according to their Fe content as a function of particle size, and Fig. 8b further displays the relative abundances of particles for each of the nine Fe categories and particle size ranges according to three Al/Si ratio categories. The Al/Si ratio is chosen because it has little measurement uncertainty, and varies significantly for different mineral groups as discussed in section ~~3.1.9~~S 2.9 of the Supplement. High Al/Si ratios indicate dominance of structural Fe-containing clay minerals, like illite, smectite and chlorite, which also tend to be internally mixed with Fe-oxi/hydroxides (Kandler et al., 2011). Low Al/Si ratios tend to be associated with quartz-like particles.

The relative ~~number~~ mass of particles with Fe fractions above 0.1 decreases with increasing particle size. Among these, particles with Fe fractions above 0.5 are hematite-like particles as shown in Fig. 8a; their relative abundance is ~ 4 % below 1 micron, which decreases steeply with size to the extent that no appreciable amounts are observed above 4 microns. Given the amount of Fe, these hematite-like particles are mostly composed of Fe-oxi/hydroxides and to first order could be taken as externally mixed Fe-oxi/hydroxide particles. However, they still show some degree of aggregation with other minerals that increase with particle size. This can be appreciated in Fig. 2, where hematite-like particles show increasing amounts of Si, Al and Mg with size. Figure 8b shows that aggregation of Fe-oxi/hydroxides (Fe > 0.5) in hematite-like particles happens mainly with clays (high Al/Si ratios), but particles with low Al/Si ratios were also observed for diameters $<$~~8~~ 4 μm. These are most likely for a fraction of particles (e.g. complex quartz-like) with some free Fe (oxy-hydr)oxides (e.g., goethite and hematite) assemblages.

Particles with Fe fractions between 0.2 and 0.5 follow a similar decrease in relative abundance with particle size although there are still appreciable amounts of particles up to 8 microns. Such particles are mostly classified as chlorite-like; in Fig. 2 chlorite particles feature Fe fractions above 0.2, and in Fig. 4 the abundance of chlorite-like particles decreases with particle

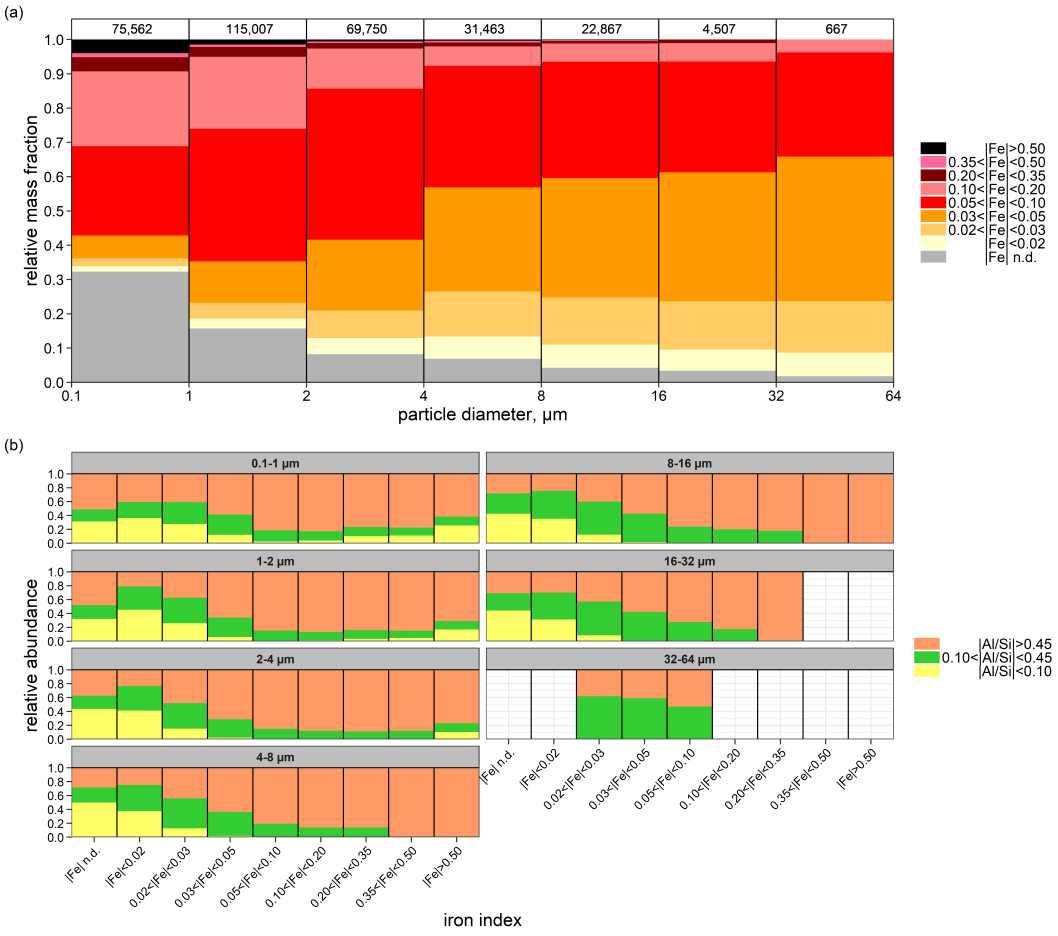

Figure 8. (a) Size resolved iron indices for silicate particles. "n.d." means Fe not detected. The numbers on top represent total particle counts in the given size bin. (b) Silicate particle with iron association based on Al/Si ratio. Abundance bars are not shown for size intervals with fewer than ~~40~~ 30 particles because of high statistical uncertainty~~and (b) Silicate particle with iron association based on Al/Si ratio~~.

size. However, the presence of Fe-oxi/hydroxide internal mixtures is very likely, particularly in particles with Fe contents towards the higher end of the 0.2-0.5 range. The relative number of particles with Fe fractions between 0.1 and 0.2 also decreases with particle size; such particles have mainly a high Al/Si ratio (clay minerals, such as illite, smectite and chlorite) (Fig. 8b). Interestingly, the relative mass abundance of particles with no Fe detected reaches ~ ~~0.38~~ 0.32 below 1 micron and thereafter also decreases with particle size. All in all, these results show that Fe-oxi/hydroxides tend to be increasingly internally mixed with other minerals, especially clays, as particle size increases. In other words, the volume fraction of Fe-oxi/hydroxides in aggregates decreases with particle size.

Conversely, with increasing particle size, the relative number of particles with Fe fractions between 0.03 - 0.05 increase, and that of particles with intermediate Fe content (0.05 - 0.10) tend to increase for particle sizes between 0.1 and 4 microns (26 %

to 44 %) while remaining approximately invariant ~~above (~~ 30 %) above 4 microns. Such increasing trends with particle size are also visible for particles with Fe contents below 0.03. The increase in particles with lower Fe content with particle size is mostly due to the increasing amount of complex clay-feldspar mixtures, complex feldspar-like and quartz-like aggregates (Fig. 4) with lower Al/Si ratios (Fig. 8b).

The mean Fe abundance is 0.09 and is dependent on size with values of 0.095 in the size range $0.1 < d < 2.5$ μm and 0.06 for particles $2.5 < d < 64$ μm. This is consistent with observations in Tinfou, Morocco (mean 0.053) for particles between 1 and 20 μm (Kandler et al., 2009). ~~The Fe relative abundance in most of the particles varies between 0.03 and 0.1, suggesting that most of the Fe are built into the crystal lattice (structural) or internally mixed as small oxide/hydroxide grains (Kandler et al., 2009; Scheuvens et al., 2011; Deboudt et al., 2012; Kandler et al., 2020).~~

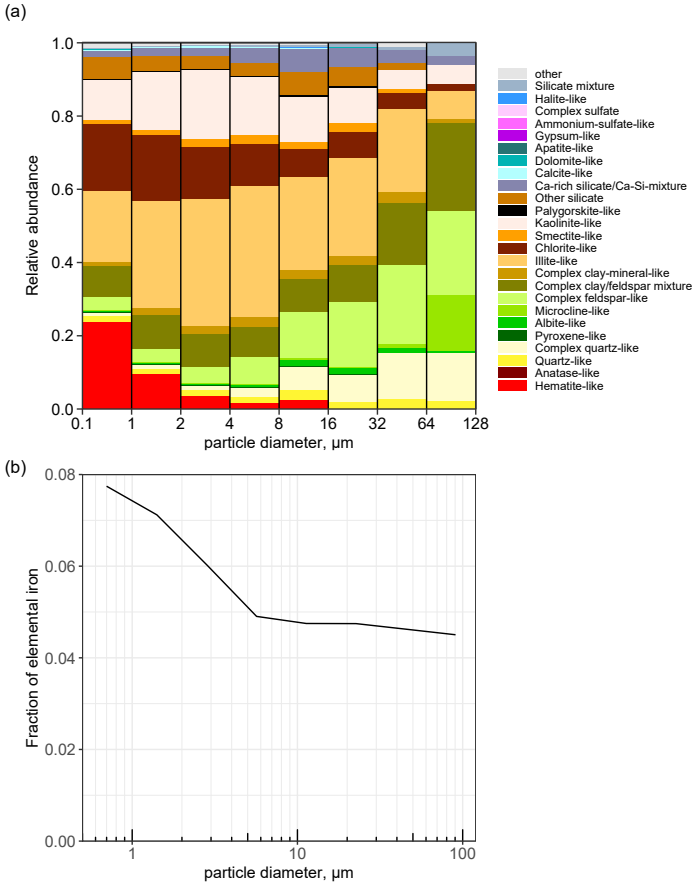

Figure 9. (a) Relative contribution of each particle type to total iron and (b) fraction of elemental iron by mass with respect to all the other elements.

Figure 9a shows the relative contribution of each particle type to Fe in every particle class. In comparison to the particle type fractions displayed in Fig. 4, the hematite-like and chlorite-like particles have an increased proportion because of their

higher contribution in terms of Fe content, and the calcite-like and Ca-rich silicate group gets substantially diminished due to the absence of Fe in carbonate minerals. It is remarkable to see that the iron contribution of clay-like aggregates (illite, smectite and kaolinite) increases with particle size up to $\sim$ 4-8 μm, which suggests (and further confirms) increased internal mixing with Fe-oxi-hydroxides. Figure 9b shows the mass fraction of elemental Fe as a function of particle size and is calculated by dividing the average estimated mass of Fe in a particle by the average estimated mass of particle. The total Fe in dust is greatly reduced with size, particularly up to $\sim$ 5 μm, going from $\sim$ 8 % below 1 micron to less than 5 % in particles above 6 μm. This is slightly higher than the values of fractional mass of elemental iron obtained for Moroccan soil using X-ray Fluorescence (XRF) analysis which was reported to be 3.6 % for $PM_{10.6}$ (Caponi et al., 2017; Di Biagio et al., 2019).

Overall, our results suggest that ~~smaller~~ fine dust particles are more enriched with Fe due to both the presence of small-sized Fe-oxi-hydroxide (hematite-like) and the increase in feldspar and quartz with particle size, which reduces the fractional abundance of clay-like particles internally mixed with Fe-oxi-hydroxides. Scheuvens et al. (2011) also observed Fe-rich particles to be relatively scarce ($<$ 1.5 % in particle number fraction). In contrast, less proportion of Fe-rich was observed from more southerly source areas (Chou et al., 2008). Usually Fe-rich particles are associated with alumosilicates (Scheuvens et al., 2011; Deboudt et a and are often located at the particle surface and has implications for particle refractive index. All these observations are complementary to the laboratory results obtained by Baddock et al. (2013) that showed abrasion from saltating particles can release Fe-rich nanoparticles from larger aggregates. As fine dust particles are more prone to long-range transport, this might provide an increased amount of soluble Fe. However, due to the association of Fe in different particle groups, it is difficult to estimate the fraction of soluble Fe available after deposition in ocean biogeochemistry and thereby the global carbon cycle or terrestrial ecosystem as a nutrient with the method used in this work. Nevertheless, as observed by Marcotte et al. (2020), the Fe solubility (% dissolved Fe/total Fe in the mineral) in pure Fe-bearing clay materials was higher by an order of magnitude than in pure Fe oxide minerals so the dust transported from this region could be a major source of nutrient.

3.3.4 Feldspar

Feldspar, and in particular K-rich feldspar, are discussed as the most efficient ice nuclei among the different mineral constituents found in dust (Atkinson et al., 2013; Harrison et al., 2016; DeMott et al., 2018) and are therefore of interest for atmospheric processes.

Figure 10 shows the feldspar relative ~~number abundance~~ mass ratio for K-feldspar and total feldspar to total particles as determined by the feldspar index approach (see Section S2.3 in the Supplement for the distinction between the two different approaches for feldspar characterization). Here the total feldspar includes K-feldspar, Na-feldspar, and other feldspar. For comparison, the ~~'classical'~~ 'relaxed' in contrast to strict classification scheme of feldspar-like particles is also shown which includes albite-like, microcline-like, anorthite-like, complex feldspar-like, and complex clay/feldspar mixture. In general, our analysis shows that approximately ~~4~~ 3 % of the dust aerosols are ~~pure~~ relatively pure, externally mixed feldspar particles whereas ~~pure~~ relatively pure, externally mixed K-feldspar particles are less than ~~1 %~~ 0.5 % by mass. With the inclusion of internally mixed feldspar, an increasing trend is observed with particle size. Studies have found the K-feldspar content of dust to be highly variable with values up to 25 % for Moroccan dust (Atkinson et al., 2013). Since the ~~size distribution~~ PSD of K-

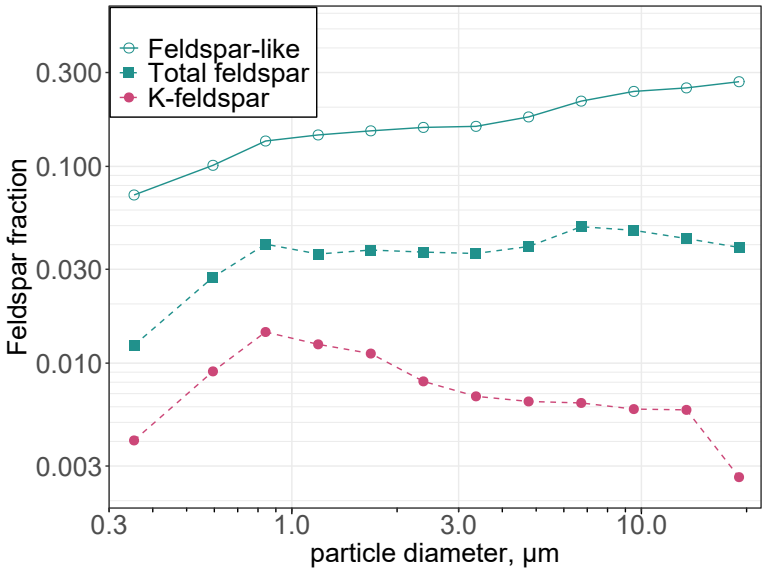

Figure 10. ~~Number~~ Mass ratio of Feldspar-like, Total feldspar (more strict criterion), and K-feldspar (more strict criterion) to total particles.

feldspar at the source determines how much of it is transported across long distances, our finding shows that the relative amount of externally mixed K-feldspar particle is size independent up to 10 μm. For long-range transported dust over Barbados, no significant variation was reported for K-feldspar under different dust conditions but are slightly lower than the values reported here using the same technique as in this study (Kandler et al., 2018; Harrison et al., 2022).

3.4 Particle shape

Dust particles were found to be highly aspherical and displayed a wide range of AR values for the size range 0.5 $<D_p<$ 100 μm, which is consistent with previous studies of Northern African dust (Chou et al., 2008; Kandler et al., 2009). The median AR of particles is 1.46 and is almost independent of particle diameter as seen in Fig. 11 (b). ~~This is consistent with the median AR (1.50) obtained by the analysis of Aerosol Robotic Network Sun photometer for dominant particles in desert dust plumes (Dubovik et al., 2006). It is however~~ It is slightly lower than the one found in previous AR measurements of Moroccan dust (median 1.6) (Kandler et al., 2009) but is similar to the Asian dust (median 1.4) (Okada et al., 2001) and those observed in Niger during aircraft campaign (Matsuki et al., 2010). These are also substantially lower than values reported for long-range transported Saharan dust (Reid et al., 2003; Coz et al., 2009). The discrepancy in observations at the point of the source region and transported dust could be the preferential removal of lower AR particles at the source due to their higher gravitational settling velocity than elongated particles of the same volume (Yang et al., 2013). Other median values found in the literature at the source location are 1.7 during African Monsoon Multidisciplinary Analysis (AMMA) campaign in Niger (Chou et al., 2008), 1.55 during Geostationary Earth Radiation Budget Intercomparisons of Longwave and Shortwave radiation (GERBILS) campaign ~~(Klaver et al., 2011). Median~~ over Mauritania, Mali and Niger (Klaver et al., 2011). A median value of

1.3 was found during the Fennec campaign in the central Sahara (Rocha-Lima et al., 2018) for particles < 5 μm and during AERosol Properties - Dust (AER-D) aircraft measurement median of 1.3-1.44 for 0.5 to 5 μm, 1.30 for 5 to 10 μm and 1.51 for 10 to 40 μm was observed ~~(Ryder et al., 2018).~~ for dust particles collected in the Saharan Air Layer and the marine boundary layer (Ryder et al., 2018). It should be noted that the AR calculation done in several of the studies mentioned are not directly comparable as systematic difference occur as function of the measurement approach (Huang et al., 2020). While the values here are corrected after Huang et al. (2020), a bias might still remain.

Table 1. Parameters of the aspect ratio density distribution, mean, median, and standard deviation for different particle classes

Particle type	σ	μ	Mean	Median	St. Dev.
Hematite-like	0.5754	-0.7942	1.51	1.44	0.30
Quartz-like	0.5917	-0.7965	1.54	1.45	0.40
Complex quartz-like	0.5991	-0.7793	1.54	1.45	0.44
Microcline-like	0.5701	-0.7263	1.53	1.46	0.30
Albite-like	0.5852	-0.7493	1.53	1.46	0.33
Complex feldspar-like	0.6204	-0.7894	1.54	1.45	0.38
Complex clay/feldspar mixture	0.5990	-0.8248	1.52	1.43	0.34
Complex clay-mineral-like	0.6008	-0.7078	1.57	1.49	0.35
Illite-like	0.5936	-0.7500	1.55	1.47	0.34
Chlorite-like	0.5928	-0.7268	1.55	1.47	0.34
Smectite-like	0.6113	-0.7390	1.55	1.46	0.35
Kaolinite-like	0.6056	-0.8136	1.52	1.44	0.35
Ca-rich silicate/Ca-Si-mixture	0.6183	-0.7006	1.58	1.50	0.40
Calcite-like	0.5904	-0.7572	1.55	1.46	0.37
Dolomite-like	0.5931	-0.9837	1.44	1.35	0.30
Gypsum-like	0.6505	-0.7287	1.60	1.46	0.49
All	0.6024	-0.7744	1.55	1.46	0.38

~~It should be noted that the AR calculation done in several of the studies mentioned above are not directly comparable as systematic difference exists due to non-uniformity in the definition of the aspect ratio as well as the software algorithms used in computing AR (Huang et al., 2020). For example the median AR of Asian dust stated as 1.4 in Okada et al. (2001) transforms to 1.68 depending on the way length and width of individual dust particles are defined (Huang et al., 2020).~~

The density distribution with respect to the AR can be parameterized by a modified log-normal distribution (Kandler et al., 2007):

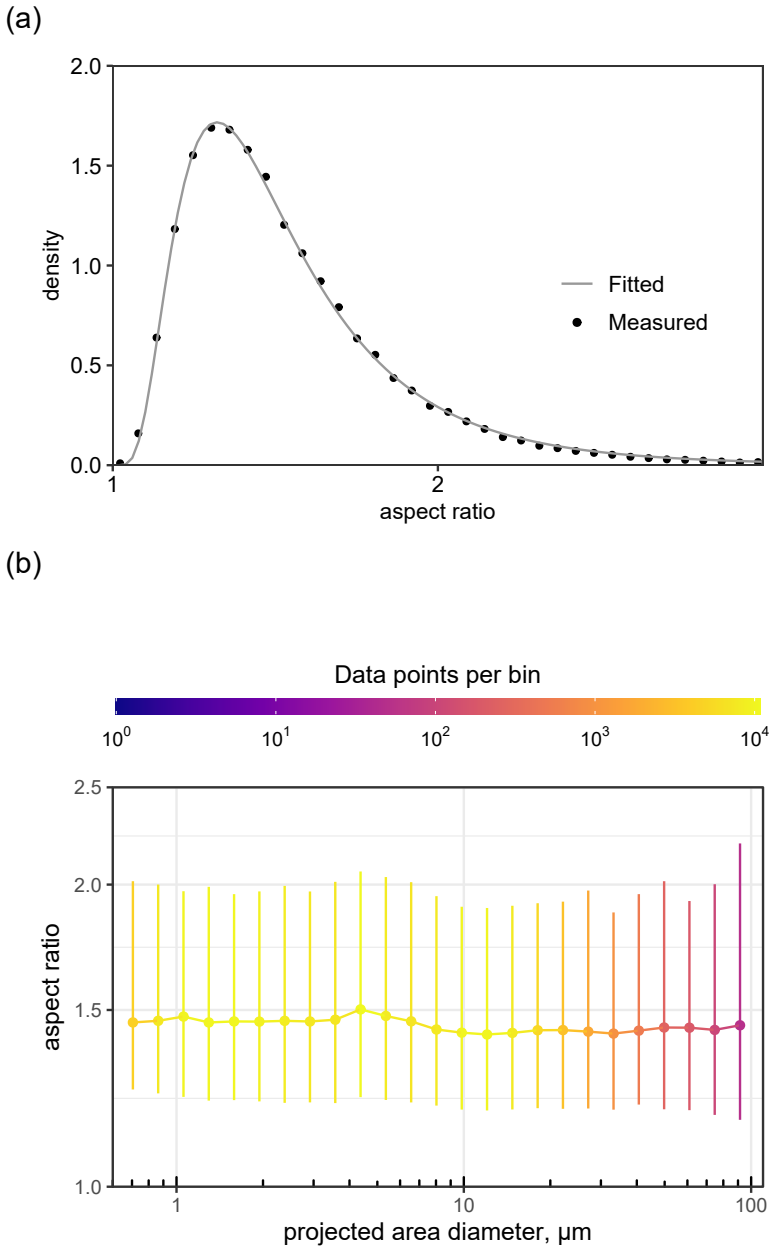

Figure 11. (a) Measured ~~(green)~~ and parameterized (~~purple~~solid line) aspect ratio density distribution of dust particles (b) Size-resolved particle aspect ratio. The ~~shaded area~~ bar range represents the range between 0.1 and 0.9 quantiles with dot being the median and the bins are color coded by the number of data points within each bin.

$$h(AR) = \frac{1}{\sqrt{2\pi} \cdot (AR-1) \cdot \sigma} \times exp\left[-\frac{1}{2}\left(\frac{ln(AR-1)-\mu}{\sigma}\right)^2\right] \quad (7)$$

~~The~~ Figure 11 (a) shows the parameterization curve together with the measured values for all particles and in Table 1 the fitting parameters σ and μ along with the median value are given ~~in Fig. 11 (a) for all particles and in table 1 for~~ for different particle classes. Most of the particle groups have a similar median AR of 1.46 except for dolomite, which has the lowest median AR of 1.35. While the AR is generally independent of particle size and particle types, slightly higher aspect ratios are observed for internally mixed particles. Differences with other locations could then be at least partly explained by differences in mineralogical composition and mixing state.

4 Conclusions

We investigated the single particle composition of freshly emitted mineral dust aerosols using SEM-EDX. Samples were collected between 4-30 September 2019 during field campaign at a major source region on the edge of the Saharan desert in Morocco (29.83 °N 5.87 °W) in the context of the FRAGMENT project. A total of more than 300,000 individual particles were classified into eight major particle classes based on their elemental composition and were: (i) oxides/hydroxides, (ii) feldspar, (iii) clay minerals, (iv) quartz-like and complex quartz-like, (v) other silicates (vi) Ca-rich, (vii) sulfates, and (viii) mixtures and others. Our analysis shows that clay minerals (illite-like, kaolinite-like) were the most abundant across the size range $d_v < 64$ μm (~~28~~ 25 %–48 % in relative ~~number~~ mass abundance). In contrast, calcite-like and chlorite-like particles were present mainly in the size range $d_v < 4$ μm, (~~4~~ 3.5 %–~~9~~ 8 %). Quartz-like particles were present in a relatively constant quantity across different size bins (~~5~~ 5.5 % –~~10~~ 8.5 %) whereas complex quartz-like particles were present primarily in the size range $d_v > 4$ μm, (~~4~~ 5 %–~~9~~ 22 %). A similarly high fraction of quartz, feldspars, and clay minerals were reported for Morocco during SAMUM (Kandler et al., 2009), except for Ca-rich particles which are significantly less in our sample whereas in Kandler et al. (2009) appear as a log-normal mode centred around 3 μm. Particles with high iron content (Fe oxides and hydroxides) were also identified which are crucial for assessing the radiative effect of mineral dust as well as are essential nutrients for marine and terrestrial ecosystems.

The time series of the overall composition of mineral dust showed relative homogeneity over the campaign. Nevertheless, elevated contents of apatite, calcite, and sulfates were observed on certain days suggesting the presence of a strong local source.

Most particle groups have median aspect ratios of around 1.46. Slightly higher aspect ratios are observed for internally-mixed particles whereas dolomite-like particles have the lowest median value of 1.35. This implies that dust aggregates with higher internal mixture fractions tend to have higher aspect ratios, which will change the radiative properties of dust. Studies have shown a trend of increasing aspect ratios for Northern African dust after transatlantic advection (Huang et al., 2020).

We provided a more exhaustive analysis of Fe-oxi/hydroxides and feldspar, including their ~~size distribution~~ PSD and potential aggregation or mixing state, which are key to the effects of dust upon radiation and clouds. Compared to clay minerals and quartz, iron-rich particles (either dominated by or externally-mixed Fe-oxi/hydroxides) are present mainly in ~~the size range~~

~~$d_v <$~~ diameters smaller than 1 μm ~~(4 % number abundance)~~at about 3.75 % abundance by mass. Our analysis suggests that Fe-oxi/hydroxides tend to be increasingly internally mixed with other minerals, especially clays, as particle size increases, with the volume fraction of Fe-oxi/hydroxides in aggregates decreasing with particle size. All in all, smaller particles are more enriched with Fe due to both the presence of Fe-oxi-hydroxide (hematite-like) and the increase in feldspar and quartz with particle size, which reduces the fractional abundance of clay-like particles internally mixed with Fe-oxi-hydroxides. The externally-mixed total feldspar and K-feldspar abundances are relatively constant in contrast to the increasing abundance of feldspar-like (internally-mixed) aggregates with particle size.

Many earth system models still assume globally uniform mineralogical composition and therefore introduce errors in the assessment of regional forcing of dust. The detailed single-particle analysis of freshly emitted dust particles in this study ~~can~~ is one key element in understanding the relationship of the emitted size-resolved composition and that of the parent soil. This important aspect will be tacked in the subsequent papers from FRAGMENT project which would help include size-resolved composition dependencies in climate models. More recent FRAGMENT field campaigns in Iceland and Jordan will supplement these measurements in understanding the source-specific mineralogical composition of dust aerosols. Recently, the field of imaging spectrometry satellite missions has progressed with the development of new instruments and projects like Earth Surface Mineral Dust Source Investigation (EMIT) (Green et al., 2020), Environmental Mapping and Analysis Program (EnMAP) (Guanter et al., 2015), and DLR Earth Sensing Imaging Spectrometer (DESIS) (Müller et al., 2016) that will retrieve global surface mineralogy. Together, all these efforts will help advance our knowledge of dust effects upon climate.

Data availability. The data presented in this paper will be made available via a public repository upon acceptance and is available for editors and reviewers during the review process.

Appendix A

Author contributions. CPG-P proposed and designed the measurement campaign with contributions from AA, KK, MK, and XQ. AP, KK, AA, CGF, AGR, MK, XQ, CR, JYD, and CPG-P implemented the field campaign. AP collected the samples, analysed them by electron microscopy, performed formal analysis, visualization (except Fig. 1 (a), and (b)), and writing of the original draft manuscript. KK and CPG-P supervised the work. AGR generated Fig. 1(a) and MK generated Fig. 1(b). KK programmed data processing code and interpretation. CPG-P re-edited the manuscript. All authors contributed in data discussion and manuscript finalization.

Competing interests. The authors declare that they have no conflict of interest.

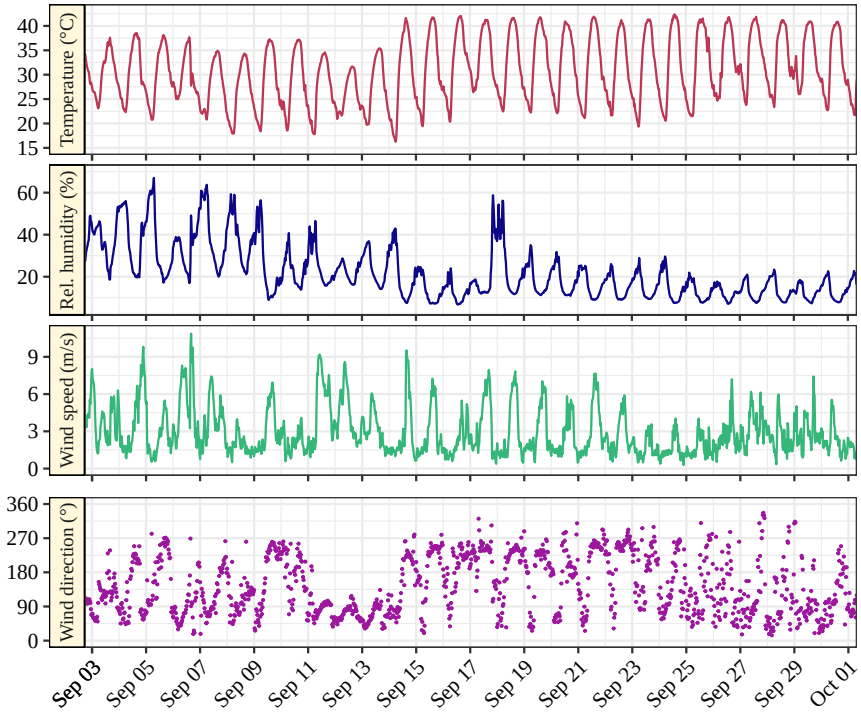

Figure A1. Time series of temperature, relative humidity, wind speed, and wind direction at approximately 2 m height. A 30 min average is applied on all time series presented.

Acknowledgements. The field campaign and its associated research, including this work, was primarily funded by the European Research Council under the Horizon 2020 research and innovation programme through the ERC Consolidator Grant FRAGMENT (grant agreement No. 773051) and the AXA Research Fund through the AXA Chair on Sand and Dust Storms at BSC. CGF was supported by a PhD fellowship from the Agència de Gestió d'Ajuts Universitaris i de Recerca (AGAUR) grant 2020_FI B 00678. KK was funded by the Deutsche Forschungsgemeinschaft (DFG, German Research Foundation) – 264907654; 416816480. MK received funding through the Helmholtz Association's Initiative and Networking Fund (grant agreement no. VH-NG-1533).

We acknowledge the EMIT project, which is supported by the NASA Earth Venture Instrument program, under the Earth Science Division of the Science Mission Directorate. We thank Dr. Santiago Beguería from the National Scientific Council of Spain for facilitating a field site in Zaragoza, Spain, to test our instrumentaltion and field procedures prior to our campaign in Morocco. We thank Prof. Kamal Taj Eddine from Cady Ayyad University, Marrakesh, Morocco for his invaluable support and suggestions for the preparation of the field campaign. We thank Houssine Dakhamat and the crew of Hotel Chez le Pacha in M'hamid El Ghizlane for their support during the campaign.

References

Adebiyi, A., Kok, J. F., Murray, B. J., Ryder, C. L., Stuut, J.-B. W., Kahn, R. A., Knippertz, P., Formenti, P., Mahowald, N. M., Pérez García-Pando, C., Klose, M., Ansmann, A., Samset, B. H., Ito, A., Balkanski, Y., Di Biagio, C., Romanias, M. N., Huang, Y., and Meng, J.: A review of coarse mineral dust in the Earth system, Aeolian Research, 60, 100 849, https://doi.org/10.1016/j.aeolia.2022.100849, 2023.

Adebiyi, A. A. and Kok, J. F.: Climate models miss most of the coarse dust in the atmosphere, Science Advances, 6, eaaz9507, https://doi.org/10.1126/sciadv.aaz9507, 2020.

Alastuey, A., Querol, X., Castillo, S., Escudero, M., Avila, A., Cuevas, E., Torres, C., Romero, P.-M., Exposito, F., García, O., Pedro Diaz, J., Dingenen, R. V., and Putaud, J. P.: Characterisation of TSP and PM2.5 at Izaña and Sta. Cruz de Tenerife (Canary Islands, Spain) during a Saharan Dust Episode (July 2002), Atmospheric Environment, 39, 4715–4728, https://doi.org/10.1016/j.atmosenv.2005.04.018, 2005.

Aluko, O. and Noll, K. E.: Deposition and Suspension of Large, Airborne Particles, Aerosol Science and Technology, 40, 503–513, https://doi.org/10.1080/02786820600664152, 2006.

Anthony, J. W., Bideaux, R. A., Bladh, K., and Nichols, M. C.: Handbook of Mineralogy, Mineralogical Society of America, Chantilly, VA 20151-1110, USA, 2003.

Atkinson, J. D., Murray, B. J., Woodhouse, M. T., Whale, T. F., Baustian, K. J., Carslaw, K. S., Dobbie, S., O'Sullivan, D., and Malkin, T. L.: The importance of feldspar for ice nucleation by mineral dust in mixed-phase clouds, Nature, 498, 355–358, https://doi.org/10.1038/nature12278, 2013.

Avila, A., Queralt-Mitjans, I., and Alarcón, M.: Mineralogical composition of African dust delivered by red rains over northeastern Spain, Journal of Geophysical Research: Atmospheres, 102, 21 977–21 996, https://doi.org/10.1029/97JD00485, 1997.

Baddock, M., Boskovic, L., Strong, C., McTainsh, G., Bullard, J., Agranovski, I., and Cropp, R.: Iron-rich nanoparticles formed by aeolian abrasion of desert dune sand, Geochemistry, Geophysics, Geosystems, 14, 3720–3729, https://doi.org/10.1002/ggge.20229, 2013.

Baker, A. R. and Jickells, T. D.: Mineral particle size as a control on aerosol iron solubility, Geophysical Research Letters, 33, https://doi.org/10.1029/2006GL026557, 2006.

Bateman, A. P., Belassein, H., and Martin, S. T.: Impactor Apparatus for the Study of Particle Rebound: Relative Humidity and Capillary Forces, Aerosol Science and Technology, 48, 42–52, https://doi.org/10.1080/02786826.2013.853866, 2014.

Blanco, A., Dee Tomasi, F., Filippo, E., Manno, D., Perrone, M. R., Serra, A., Tafuro, A. M., and Tepore, A.: Characterization of African dust over southern Italy, Atmospheric Chemistry and Physics, 3, 2147–2159, https://doi.org/10.5194/acp-3-2147-2003, 2003.

Caponi, L., Formenti, P., Massabó, D., Di Biagio, C., Cazaunau, M., Pangui, E., Chevaillier, S., Landrot, G., Andreae, M. O., Kandler, K., Piketh, S., Saeed, T., Seibert, D., Williams, E., Balkanski, Y., Prati, P., and Doussin, J.-F.: Spectral- and size-resolved mass absorption efficiency of mineral dust aerosols in the shortwave spectrum: a simulation chamber study, Atmospheric Chemistry and Physics, 17, 7175–7191, https://doi.org/10.5194/acp-17-7175-2017, 2017.

Choobari, O. A., Zawar-Reza, P., and Sturman, A.: The global distribution of mineral dust and its impacts on the climate system: A review, Atmospheric Research, 138, 152–165, https://doi.org/10.1016/j.atmosres.2013.11.007, 2014.

Chou, C., Formenti, P., Maille, M., Ausset, P., Helas, G., Harrison, M., and Osborne, S.: Size distribution, shape, and composition of mineral dust aerosols collected during the African Monsoon Multidisciplinary Analysis Special Observation Period 0: Dust and Biomass-Burning Experiment field campaign in Niger, January 2006, Journal of Geophysical Research: Atmospheres, 113, https://doi.org/10.1029/2008JD009897, 2008.

Claquin, T., Schulz, M., and Balkanski, Y. J.: Modeling the mineralogy of atmospheric dust sources, Journal of Geophysical Research: Atmospheres, 104, 22 243–22 256, https://doi.org/doi.org/10.1029/1999JD900416, 1999.

Coz, E., Gómez-Moreno, F. J., Pujadas, M., Casuccio, G. S., Lersch, T. L., and Artíñano, B.: Individual particle characteristics of North African dust under different long-range transport scenarios, Atmospheric Environment, 43, 1850–1863, https://doi.org/10.1016/j.atmosenv.2008.12.045, 2009.

Cwiertny, D. M., Young, M. A., and Grassian, V. H.: Chemistry and Photochemistry of Mineral Dust Aerosol, Annual Review of Physical Chemistry, 59, 27–51, https://doi.org/10.1146/annurev.physchem.59.032607.093630, pMID: 18393675, 2008.

Deboudt, K., Gloter, A., Mussi, A., and Flament, P.: Red-ox speciation and mixing state of iron in individual African dust particles, Journal of Geophysical Research: Atmospheres, 117, https://doi.org/10.1029/2011JD017298, 2012.

DeMott, P. J., Möhler, O., Cziczo, D. J., Hiranuma, N., Petters, M. D., Petters, S. S., Belosi, F., Bingemer, H. G., Brooks, S. D., Budke, C., Burkert-Kohn, M., Collier, K. N., Danielczok, A., Eppers, O., Felgitsch, L., Garimella, S., Grothe, H., Herenz, P., Hill, T. C. J., Höhler, K., Kanji, Z. A., Kiselev, A., Koop, T., Kristensen, T. B., Krüger, K., Kulkarni, G., Levin, E. J. T., Murray, B. J., Nicosia, A., OŚullivan, D., Peckhaus, A., Polen, M. J., Price, H. C., Reicher, N., Rothenberg, D. A., Rudich, Y., Santachiara, G., Schiebel, T., Schrod, J., Seifried, T. M., Stratmann, F., Sullivan, R. C., Suski, K. J., Szakáll, M., Taylor, H. P., Ullrich, R., Vergara-Temprado, J., Wagner, R., Whale, T. F., Weber, D., Welti, A., Wilson, T. W., Wolf, M. J., and Zenker, J.: The Fifth International Workshop on Ice Nucleation phase 2 (FIN-02): laboratory intercomparison of ice nucleation measurements, Atmospheric Measurement Techniques, 11, 6231–6257, https://doi.org/10.5194/amt-11-6231-2018, 2018.

Di Biagio, C., Formenti, P., Balkanski, Y., Caponi, L., Cazaunau, M., Pangui, E., Journet, E., Nowak, S., Andreae, M. O., Kandler, K., Saeed, T., Piketh, S., Seibert, D., Williams, E., and Doussin, J.-F.: Complex refractive indices and single-scattering albedo of global dust aerosols in the shortwave spectrum and relationship to size and iron content, Atmospheric Chemistry and Physics, 19, 15 503–15 531, https://doi.org/10.5194/acp-19-15503-2019, 2019.

Dubovik, O., Sinyuk, A., Lapyonok, T., Holben, B. N., Mishchenko, M., Yang, P., Eck, T. F., Volten, H., Muñoz, O., Veihelmann, B., van der Zande, W. J., Leon, J.-F., Sorokin, M., and Slutsker, I.: Application of spheroid models to account for aerosol particle nonsphericity in remote sensing of desert dust, Journal of Geophysical Research: Atmospheres, 111, https://doi.org/10.1029/2005JD006619, 2006.

Ebert, M., Dahmen, J., Hoffmann, P., and Ortner, H.: Examination of clean room aerosol particle composition by total reflection X-ray analysis and electron probe microanalysis, Spectrochimica Acta Part B: Atomic Spectroscopy, 52, 967–975, https://doi.org/10.1016/S0584-8547(96)01634-5, 1997.

Engelbrecht, J. P., McDonald, E. V., Gillies, J. A., Jayanty, R. K. J., Casuccio, G., and Gertler, A. W.: Characterizing Mineral Dusts and Other Aerosols from the Middle East—Part 2: Grab Samples and Re-Suspensions, Inhalation Toxicology, 21, 327–336, https://doi.org/10.1080/08958370802464299, 2009a.

Engelbrecht, J. P., McDonald, E. V., Gillies, J. A., Jayanty, R. K. M., Casuccio, G., and Gertler, A. W.: Characterizing Mineral Dusts and Other Aerosols from the Middle East—Part 1: Ambient Sampling, Inhalation Toxicology, 21, 297–326, https://doi.org/10.1080/08958370802464273, 2009b.

Engelbrecht, J. P., Moosmüller, H., Pincock, S., Jayanty, R. K. M., Lersch, T., and Casuccio, G.: Technical note: Mineralogical, chemical, morphological, and optical interrelationships of mineral dust re-suspensions, Atmospheric Chemistry and Physics, 16, 10 809–10 830, https://doi.org/10.5194/acp-16-10809-2016, 2016.

Engelbrecht, J. P., Stenchikov, G., Prakash, P. J., Lersch, T., Anisimov, A., and Shevchenko, I.: Physical and chemical properties of deposited airborne particulates over the Arabian Red Sea coastal plain, Atmospheric Chemistry and Physics, 17, 11 467–11 490, https://doi.org/10.5194/acp-17-11467-2017, 2017.

Engelstaedter, S., Tegen, I., and Washington, R.: North African dust emissions and transport, Earth-Science Reviews, 79, 73–100, https://doi.org/10.1016/j.earscirev.2006.06.004, 2006.

Fang, C. P., McMurry, P. H., Marple, V. A., and Rubow, K. L.: Effect of Flow-induced Relative Humidity Changes on Size Cuts for Sulfuric Acid Droplets in the Microorifice Uniform Deposit Impactor (MOUDI), Aerosol Science and Technology, 14, 266–277, https://doi.org/10.1080/02786829108959489, 1991.

Fitzgerald, E., Ault, A. P., Zauscher, M. D., Mayol-Bracero, O. L., and Prather, K. A.: Comparison of the mixing state of long-range transported Asian and African mineral dust, Atmospheric Environment, 115, 19–25, https://doi.org/10.1016/j.atmosenv.2015.04.031, 2015.

Formenti, P., Schütz, L., Balkanski, Y., Desboeufs, K., Ebert, M., Kandler, K., Petzold, A., Scheuvens, D., Weinbruch, S., and Zhang, D.: Recent progress in understanding physical and chemical properties of African and Asian mineral dust, Atmospheric Chemistry and Physics, 11, 8231–8256, https://doi.org/10.5194/acp-11-8231-2011, 2011.

Froyd, K. D., Yu, P., Schill, G. P., Brock, C. A., Kupc, A., Williamson, C. J., Jensen, E. J., Ray, E., Rosenlof, K. H., Bian, H., et al.: Dominant role of mineral dust in cirrus cloud formation revealed by global-scale measurements, Nature Geoscience, 15, 177–183, https://doi.org/10.1038/s41561-022-00901-w, 2022.

Giannadaki, D., Pozzer, A., and Lelieveld, J.: Modeled global effects of airborne desert dust on air quality and premature mortality, Atmospheric Chemistry and Physics, 14, 957–968, https://doi.org/10.5194/acp-14-957-2014, 2014.

Ginoux, P.: Effects of nonsphericity on mineral dust modeling, Journal of Geophysical Research: Atmospheres, 108, https://doi.org/10.1029/2002JD002516, 2003.

Ginoux, P., Prospero, J. M., Gill, T. E., Hsu, N. C., and Zhao, M.: Global-scale attribution of anthropogenic and natural dust sources and their emission rates based on MODIS Deep Blue aerosol products, Reviews of Geophysics, 50, https://doi.org/10.1029/2012RG000388, 2012.

Gliß, J., Mortier, A., Schulz, M., Andrews, E., Balkanski, Y., Bauer, S. E., Benedictow, A. M. K., Bian, H., Checa-Garcia, R., Chin, M., Ginoux, P., Griesfeller, J. J., Heckel, A., Kipling, Z., Kirkevåg, A., Kokkola, H., Laj, P., Le Sager, P., Lund, M. T., Lund Myhre, C., Matsui, H., Myhre, G., Neubauer, D., van Noije, T., North, P., Olivié, D. J. L., Rémy, S., Sogacheva, L., Takemura, T., Tsigaridis, K., and Tsyro, S. G.: AeroCom phase III multi-model evaluation of the aerosol life cycle and optical properties using ground- and space-based remote sensing as well as surface in situ observations, Atmospheric Chemistry and Physics, 21, 87–128, https://doi.org/10.5194/acp-21-87-2021, 2021.

González-Flórez, C., Klose, M., Alastuey, A., Dupont, S., Escribano, J., Etyemezian, V., Gonzalez-Romero, A., Huang, Y., Kandler, K., Nikolich, G., Panta, A., Querol, X., Reche, C., Yus-Díez, J., and Pérez García-Pando, C.: Insights into the size-resolved dust emission from field measurements in the Moroccan Sahara, Atmospheric Chemistry and Physics Discussions, 2022, 1–65, https://doi.org/10.5194/acp-2022-758, 2022.

González-Romero, A., Querol, X., Alastuey, A., González-Flórez, C., Kandler, K., Klose, M., Panta, A., Reche, C., Yús-Díez, J., and Perez García-Pando, C.: Properties of dust-source sediment and their importance on dust emission: a local example in S Morocco, in prep.

Green, R. O., Mahowald, N., Ung, C., Thompson, D. R., Bator, L., Bennet, M., Bernas, M., Blackway, N., Bradley, C., Cha, J., Clark, P., Clark, R., Cloud, D., Diaz, E., Ben Dor, E., Duren, R., Eastwood, M., Ehlmann, B. L., Fuentes, L., Ginoux, P., Gross, J., He, Y., Kalashnikova, O., Kert, W., Keymeulen, D., Klimesh, M., Ku, D., Kwong-Fu, H., Liggett, E., Li, L., Lundeen, S., Makowski, M. D., Mazer, A., Miller, R., Mouroulis, P., Oaida, B., Okin, G. S., Ortega, A., Oyake, A., Nguyen, H., Pace, T., Painter, T. H., Pempejian, J.,

Garcia-Pando, C. P., Pham, T., Phillips, B., Pollock, R., Purcell, R., Realmuto, V., Schoolcraft, J., Sen, A., Shin, S., Shaw, L., Soriano, M., Swayze, G., Thingvold, E., Vaid, A., and Zan, J.: The Earth Surface Mineral Dust Source Investigation: An Earth Science Imaging Spectroscopy Mission, in: 2020 IEEE Aerospace Conference, pp. 1–15, https://doi.org/10.1109/AERO47225.2020.9172731, 2020.

Guanter, L., Kaufmann, H., Segl, K., Foerster, S., Rogass, C., Chabrillat, S., Kuester, T., Hollstein, A., Rossner, G., Chlebek, C., Straif, C., Fischer, S., Schrader, S., Storch, T., Heiden, U., Mueller, A., Bachmann, M., Mühle, H., Müller, R., Habermeyer, M., Ohndorf, A., Hill, J., Buddenbaum, H., Hostert, P., Van der Linden, S., Leitão, P. J., Rabe, A., Doerffer, R., Krasemann, H., Xi, H., Mauser, W., Hank, T., Locherer, M., Rast, M., Staenz, K., and Sang, B.: The EnMAP Spaceborne Imaging Spectroscopy Mission for Earth Observation, Remote Sensing, 7, 8830–8857, https://doi.org/10.3390/rs70708830, 2015.

Harrison, A. D., Whale, T. F., Carpenter, M. A., Holden, M. A., Neve, L., OSullivan, D., Vergara Temprado, J., and Murray, B. J.: Not all feldspars are equal: a survey of ice nucleating properties across the feldspar group of minerals, Atmospheric Chemistry and Physics, 16, 10 927–10 940, https://doi.org/10.5194/acp-16-10927-2016, 2016.

Harrison, A. D., O'Sullivan, D., Adams, M. P., Porter, G. C. E., Blades, E., Brathwaite, C., Chewitt-Lucas, R., Gaston, C., Hawker, R., Krüger, O. O., Neve, L., Pöhlker, M. L., Pöhlker, C., Pöschl, U., Sanchez-Marroquin, A., Sealy, A., Sealy, P., Tarn, M. D., Whitehall, S., McQuaid, J. B., Carslaw, K. S., Prospero, J. M., and Murray, B. J.: The ice-nucleating activity of African mineral dust in the Caribbean boundary layer, Atmospheric Chemistry and Physics, 22, 9663–9680, https://doi.org/10.5194/acp-22-9663-2022, 2022.

Hartung, J., Elpelt, B., and Klösener, K.-H.: Statistik: Lehr- und Handbuch der angewandten Statistik, Oldenbourg Wissenschaftsverlag, https://doi.org/10.1524/9783486710540, 2012.

Hettiarachchi, E., Ivanov, S., Kieft, T., Goldstein, H. L., Moskowitz, B. M., Reynolds, R. L., and Rubasinghege, G.: Atmospheric Processing of Iron-Bearing Mineral Dust Aerosol and Its Effect on Growth of a Marine Diatom, Cyclotella meneghiniana, Environmental Science & Technology, 55, 871–881, https://doi.org/10.1021/acs.est.0c06995, 2021.

Hoose, C. and Möhler, O.: Heterogeneous ice nucleation on atmospheric aerosols: a review of results from laboratory experiments, Atmospheric Chemistry and Physics, 12, 9817–9854, https://doi.org/10.5194/acp-12-9817-2012, 2012.

Huang, Y., Kok, J. F., Kandler, K., Lindqvist, H., Nousiainen, T., Sakai, T., Adebiyi, A., and Jokinen, O.: Climate Models and Remote Sensing Retrievals Neglect Substantial Desert Dust Asphericity, Geophysical Research Letters, 47, e2019GL086 592, https://doi.org/10.1029/2019GL086592, 2020.

Ito, A., Adebiyi, A. A., Huang, Y., and Kok, J. F.: Less atmospheric radiative heating by dust due to the synergy of coarser size and aspherical shape, Atmospheric Chemistry and Physics, 21, 16 869–16 891, https://doi.org/10.5194/acp-21-16869-2021, 2021.

Jeong, G. Y.: Bulk and single-particle mineralogy of Asian dust and a comparison with its source soils, Journal of Geophysical Research: Atmospheres, 113, https://doi.org/10.1029/2007JD008606, 2008.

Jickells, T. D., An, Z. S., Andersen, K. K., Baker, A. R., Bergametti, G., Brooks, N., Cao, J. J., Boyd, P. W., Duce, R. A., Hunter, K. A., Kawahata, H., Kubilay, N., laRoche, J., Liss, P. S., Mahowald, N., Prospero, J. M., Ridgwell, A. J., Tegen, I., and Torres, R.: Global Iron Connections Between Desert Dust, Ocean Biogeochemistry, and Climate, Science, 308, 67–71, https://doi.org/10.1126/science.1105959, 2005.

Jish Prakash, P., Stenchikov, G., Tao, W., Yapici, T., Warsama, B., and Engelbrecht, J. P.: Arabian Red Sea coastal soils as potential mineral dust sources, Atmospheric Chemistry and Physics, 16, 11 991–12 004, https://doi.org/10.5194/acp-16-11991-2016, 2016.

Journet, E., Balkanski, Y., and Harrison, S. P.: A new data set of soil mineralogy for dust-cycle modeling, Atmospheric Chemistry and Physics, 14, 3801–3816, https://doi.org/10.5194/acp-14-3801-2014, 2014.

Kaaden, N., Massling, A., Schladitz, A., Müller, T., Kandler, K., Schütz, L., Weinzierl, B., Petzold, A., Tesche, M., Leinert, S., Deutscher, C., Ebert, M., Weinbruch, S., and Wiedensohler, A.: State of mixing, shape factor, number size distribution, and hygroscopic growth of the Saharan anthropogenic and mineral dust aerosol at Tinfou, Morocco, Tellus B: Chemical and Physical Meteorology, 61, 51–63, https://doi.org/10.1111/j.1600-0889.2008.00388.x, 2009.

Kandler, K., Benker, N., Bundke, U., Cuevas, E., Ebert, M., Knippertz, P., Rodríguez, S., Schütz, L., and Weinbruch, S.: Chemical composition and complex refractive index of Saharan Mineral Dust at Izaña, Tenerife (Spain) derived by electron microscopy, Atmospheric Environment, 41, 8058–8074, https://doi.org/10.1016/j.atmosenv.2007.06.047, 2007.

Kandler, K., Schütz, L., Deutscher, C., Ebert, M., Hofmann, H., Jäckel, S., Jaenicke, R., Knippertz, P., Lieke, K., Massling, A., Petzold, A., Schladitz, A., Weinzierl, B., Wiedensohler, A., Zorn, S., and Weinbruch, S.: Size distribution, mass concentration, chemical and mineralogical composition and derived optical parameters of the boundary layer aerosol at Tinfou, Morocco, during SAMUM 2006, Tellus B: Chemical and Physical Meteorology, 61, 32–50, https://doi.org/10.1111/j.1600-0889.2008.00385.x, 2009.

Kandler, K., Lieke, K., Benker, N., Emmel, C., Küpper, M., Müller-Ebert, D., Ebert, M., Scheuvens, D., Schladitz, A., Schütz, L., and Weinbruch, S.: Electron microscopy of particles collected at Praia, Cape Verde, during the Saharan Mineral Dust Experiment: particle chemistry, shape, mixing state and complex refractive index, Tellus B: Chemical and Physical Meteorology, 63, 475–496, https://doi.org/10.1111/j.1600-0889.2011.00550.x, 2011.

Kandler, K., Schneiders, K., Ebert, M., Hartmann, M., Weinbruch, S., Prass, M., and Pöhlker, C.: Composition and mixing state of atmospheric aerosols determined by electron microscopy: method development and application to aged Saharan dust deposition in the Caribbean boundary layer, Atmospheric Chemistry and Physics, 18, 13 429–13 455, https://doi.org/10.5194/acp-18-13429-2018, 2018.

Kandler, K., Schneiders, K., Heuser, J., Waza, A., Aryasree, S., Althausen, D., Hofer, J., Abdullaev, S. F., and Makhmudov, A. N.: Differences and Similarities of Central Asian, African, and Arctic Dust Composition from a Single Particle Perspective, Atmosphere, 11, https://doi.org/10.3390/atmos11030269, 2020.

Kiselev, A., Bachmann, F., Pedevilla, P., Cox, S. J., Michaelides, A., Gerthsen, D., and Leisner, T.: Active sites in heterogeneous ice nucleation - the example of K-rich feldspars, Science, 355, 367–371, https://doi.org/10.1126/science.aai8034, 2017.

Klaver, A., Formenti, P., Caquineau, S., Chevaillier, S., Ausset, P., Calzolai, G., Osborne, S., Johnson, B., Harrison, M., and Dubovik, O.: Physico-chemical and optical properties of Sahelian and Saharan mineral dust: in situ measurements during the GERBILS campaign, Quarterly Journal of the Royal Meteorological Society, 137, 1193–1210, https://doi.org/10.1002/qj.889, 2011.

Klose, M., Jorba, O., Gonçalves Ageitos, M., Escribano, J., Dawson, M. L., Obiso, V., Di Tomaso, E., Basart, S., Montané Pinto, G., Macchia, F., Ginoux, P., Guerschman, J., Prigent, C., Huang, Y., Kok, J. F., Miller, R. L., and Pérez García-Pando, C.: Mineral dust cycle in the Multiscale Online Nonhydrostatic AtmospheRe CHemistry model (MONARCH) Version 2.0, Geoscientific Model Development, 14, 6403–6444, https://doi.org/10.5194/gmd-14-6403-2021, 2021.

Kok, J. F.: A scaling theory for the size distribution of emitted dust aerosols suggests climate models underestimate the size of the global dust cycle, Proceedings of the National Academy of Sciences, 108, 1016–1021, https://doi.org/10.1073/pnas.1014798108, 2011.

Kok, J. F., Adebiyi, A. A., Albani, S., Balkanski, Y., Checa-Garcia, R., Chin, M., Colarco, P. R., Hamilton, D. S., Huang, Y., Ito, A., Klose, M., Li, L., Mahowald, N. M., Miller, R. L., Obiso, V., Pérez García-Pando, C., Rocha-Lima, A., and Wan, J. S.: Contribution of the worldś main dust source regions to the global cycle of desert dust, Atmospheric Chemistry and Physics, 21, 8169–8193, https://doi.org/10.5194/acp-21-8169-2021, 2021.

Kok, J. F., Adebiyi, A. A., Albani, S., Balkanski, Y., Checa-Garcia, R., Chin, M., Colarco, P. R., Hamilton, D. S., Huang, Y., Ito, A., Klose, M., Leung, D. M., Li, L., Mahowald, N. M., Miller, R. L., Obiso, V., Pérez García-Pando, C., Rocha-Lima, A., Wan, J. S., and Whicker,

C. A.: Improved representation of the global dust cycle using observational constraints on dust properties and abundance, Atmospheric Chemistry and Physics, 21, 8127–8167, https://doi.org/10.5194/acp-21-8127-2021, 2022.

Kumar, P., Sokolik, I. N., and Nenes, A.: Cloud condensation nuclei activity and droplet activation kinetics of wet processed regional dust samples and minerals, Atmospheric Chemistry and Physics, 11, 8661–8676, https://doi.org/10.5194/acp-11-8661-2011, 2011.

Lafon, S., Sokolik, I. N., Rajot, J. L., Caquineau, S., and Gaudichet, A.: Characterization of iron oxides in mineral dust aerosols: Implications for light absorption, Journal of Geophysical Research: Atmospheres, 111, https://doi.org/10.1029/2005JD007016, 2006.

Li, J. and Osada, K.: Preferential settling of elongated mineral dust particles in the atmosphere, Geophysical Research Letters, 34, https://doi.org/10.1029/2007GL030262, 2007.

Li, L., Mahowald, N. M., Miller, R. L., Pérez García-Pando, C., Klose, M., Hamilton, D. S., Gonçalves Ageitos, M., Ginoux, P., Balkanski, Y., Green, R. O., Kalashnikova, O., Kok, J. F., Obiso, V., Paynter, D., and Thompson, D. R.: Quantifying the range of the dust direct radiative effect due to source mineralogy uncertainty, Atmospheric Chemistry and Physics, 21, 3973–4005, https://doi.org/10.5194/acp-21-3973-2021, 2021.

Lindqvist, H., Jokinen, O., Kandler, K., Scheuvens, D., and Nousiainen, T.: Single scattering by realistic, inhomogeneous mineral dust particles with stereogrammetric shapes, Atmospheric Chemistry and Physics, 14, 143–157, https://doi.org/10.5194/acp-14-143-2014, 2014.

Liu, D., Taylor, J. W., Crosier, J., Marsden, N., Bower, K. N., Lloyd, G., Ryder, C. L., Brooke, J. K., Cotton, R., Marenco, F., Blyth, A., Cui, Z., Estelles, V., Gallagher, M., Coe, H., and Choularton, T. W.: Aircraft and ground measurements of dust aerosols over the west African coast in summer 2015 during ICE-D and AER-D, Atmospheric Chemistry and Physics, 18, 3817–3838, https://doi.org/10.5194/acp-18-3817-2018, 2018.

Mahowald, N., Albani, S., Kok, J. F., Engelstaeder, S., Scanza, R., Ward, D. S., and Flanner, M. G.: The size distribution of desert dust aerosols and its impact on the Earth system, Aeolian Research, 15, 53–71, https://doi.org/10.1016/j.aeolia.2013.09.002, 2014.

Mahowald, N. M., Engelstaedter, S., Luo, C., Sealy, A., Artaxo, P., Benitez-Nelson, C., Bonnet, S., Chen, Y., Chuang, P. Y., Cohen, D. D., Dulac, F., Herut, B., Johansen, A. M., Kubilay, N., Losno, R., Maenhaut, W., Paytan, A., Prospero, J. M., Shank, L. M., and Siefert, R. L.: Atmospheric Iron Deposition: Global Distribution, Variability, and Human Perturbations, Annual Review of Marine Science, 1, 245–278, https://doi.org/10.1146/annurev.marine.010908.163727, pMID: 21141037, 2009.

Mallios, S. A., Drakaki, E., and Amiridis, V.: Effects of dust particle sphericity and orientation on their gravitational settling in the earth's atmosphere, Journal of Aerosol Science, 150, 105 634, https://doi.org/10.1016/j.jaerosci.2020.105634, 2020.

Marcotte, A. R., Anbar, A. D., Majestic, B. J., and Herckes, P.: Mineral Dust and Iron Solubility: Effects of Composition, Particle Size, and Surface Area, Atmosphere, 11, https://doi.org/10.3390/atmos11050533, 2020.

Marsden, N. A., Ullrich, R., Möhler, O., Eriksen Hammer, S., Kandler, K., Cui, Z., Williams, P. I., Flynn, M. J., Liu, D., Allan, J. D., and Coe, H.: Mineralogy and mixing state of north African mineral dust by online single-particle mass spectrometry, Atmospheric Chemistry and Physics, 19, 2259–2281, https://doi.org/10.5194/acp-19-2259-2019, 2019.

Matsuki, A., Schwarzenboeck, A., Venzac, H., Laj, P., Crumeyrolle, S., and Gomes, L.: Cloud processing of mineral dust: direct comparison of cloud residual and clear sky particles during AMMA aircraft campaign in summer 2006, Atmospheric Chemistry and Physics, 10, 1057–1069, https://doi.org/10.5194/acp-10-1057-2010, 2010.

Middleton, N.: Desert dust hazards: A global review, Aeolian Research, 24, 53–63, https://doi.org/10.1016/j.aeolia.2016.12.001, 2017.

Mishchenko, M. I., Travis, L. D., Kahn, R. A., and West, R. A.: Modeling phase functions for dustlike tropospheric aerosols using a shape mixture of randomly oriented polydisperse spheroids, Journal of Geophysical Research: Atmospheres, 102, 16 831–16 847, https://doi.org/10.1029/96JD02110, 1997.

Monteiro, A., Basart, S., Kazadzis, S., Votsis, A., Gkikas, A., Vandenbussche, S., Tobias, A., Gama, C., García-Pando, C. P., Terradellas, E., Notas, G., Middleton, N., Kushta, J., Amiridis, V., Lagouvardos, K., Kosmopoulos, P., Kotroni, V., Kanakidou, M., Mihalopoulos, N., Kalivitis, N., Dagsson-Waldhauserová, P., El-Askary, H., Sievers, K., Giannaros, T., Mona, L., Hirtl, M., Skomorowski, P., Virtanen, T. H., Christoudias, T., Di Mauro, B., Trippetta, S., Kutuzov, S., Meinander, O., and Nickovic, S.: Multi-sectoral impact assessment of an extreme African dust episode in the Eastern Mediterranean in March 2018, Science of The Total Environment, 843, 156 861, https://doi.org/10.1016/j.scitotenv.2022.156861, 2022.

Moosmüller, H., Engelbrecht, J. P., Skiba, M., Frey, G., Chakrabarty, R. K., and Arnott, W. P.: Single scattering albedo of fine mineral dust aerosols controlled by iron concentration, Journal of Geophysical Research: Atmospheres, 117, https://doi.org/10.1029/2011JD016909, 2012.

Moskowitz, B. M., Reynolds, R. L., Goldstein, H. L., Berquó, T. S., Kokaly, R. F., and Bristow, C. S.: Iron oxide minerals in dust-source sediments from the Bodélé Depression, Chad: Implications for radiative properties and Fe bioavailability of dust plumes from the Sahara, Aeolian Research, 22, 93–106, https://doi.org/10.1016/j.aeolia.2016.07.001, 2016.

Müller, R., Avbelj, J., Carmona, E., Gerasch, B., Graham, L., Günther, B., Heiden, U., Kerr, G., Knodt, U., Krutz, D., et al.: The new hyperspectral sensor DESIS on the multi-payload platform MUSES installed on the ISS, The International Archives of the Photogrammetry, Remote Sensing and Spatial Information Sciences, 41, 461–467, 2016.

Myriokefalitakis, S., Bergas-Massó, E., Gonçalves-Ageitos, M., Pérez García-Pando, C., van Noije, T., Le Sager, P., Ito, A., Athanasopoulou, E., Nenes, A., Kanakidou, M., Krol, M. C., and Gerasopoulos, E.: Multiphase processes in the EC-Earth model and their relevance to the atmospheric oxalate, sulfate, and iron cycles, Geoscientific Model Development, 15, 3079–3120, https://doi.org/10.5194/gmd-15-3079-2022, 2022.

Müller, D., Heinold, B., Tesche, M., Tegen, I., Althausen, D., Arboledas, L. A., Amiridis, V., Amodeo, A., Ansmann, A., Balis, D., Comeron, A., D'mico, G., Gerasopoulos, E., Guerrero-Rascado, J., Freudenthaler, V., Giannakaki, E., Heese, B., Iarlori, M., Knippertz, P., Mamouri, R., Mona, L., Papayannis, A., Pappalardo, G., Perrone, R.-M., Pisani, G., Rizi, V., Sicard, M., Spinelli, N., Tafuro, A., and Wiegner, M.: EARLINET observations of the 14–22-May long-range dust transport event during SAMUM 2006: validation of results from dust transport modelling, Tellus B: Chemical and Physical Meteorology, 61, 325–339, https://doi.org/10.1111/j.1600-0889.2008.00400.x, 2009.

Ndour, M., DÁnna, B., George, C., Ka, O., Balkanski, Y., Kleffmann, J., Stemmler, K., and Ammann, M.: Photoenhanced uptake of NO2 on mineral dust: Laboratory experiments and model simulations, Geophysical Research Letters, 35, https://doi.org/10.1029/2007GL032006, 2008.

Nickovic, S., Vukovic, A., Vujadinovic, M., Djurdjevic, V., and Pejanovic, G.: Technical Note: High-resolution mineralogical database of dust-productive soils for atmospheric dust modeling, Atmospheric Chemistry and Physics, 12, 845–855, https://doi.org/10.5194/acp-12-845-2012, 2012.

Noll, K. E., Jackson, M. M., and Oskouie, A. K.: Development of an Atmospheric Particle Dry Deposition Model, Aerosol Science and Technology, 35, 627–636, https://doi.org/10.1080/02786820119835, 2001.

Nousiainen, T. and Kandler, K.: Light scattering by atmospheric mineral dust particles, in: Light Scattering Reviews 9, pp. 3–52, Springer, https://doi.org/10.1007/978-3-642-37985-7_1, 2015.

Nousiainen, T., Kahnert, M., and Lindqvist, H.: Can particle shape information be retrieved from light-scattering observations using spheroidal model particles?, Journal of Quantitative Spectroscopy and Radiative Transfer, 112, 2213–2225, https://doi.org/10.1016/j.jqsrt.2011.05.008, polarimetric Detection, Characterization, and Remote Sensing, 2011.

Okada, K., Heintzenberg, J., Kai, K., and Qin, Y.: Shape of atmospheric mineral particles collected in three Chinese arid-regions, Geophysical Research Letters, 28, 3123–3126, https://doi.org/10.1029/2000GL012798, 2001.

Ott, D. K. and Peters, T. M.: A Shelter to Protect a Passive Sampler for Coarse Particulate Matter, PM10 - 2.5, Aerosol Science and Technology, 42, 299–309, https://doi.org/10.1080/02786820802054236, 2008.

Otto, S., Bierwirth, E., Weinzierl, B., Kandler, K., Esselborn, M., Tesche, M., Schladitz, A., Wendisch, M., and Trautmann, T.: Solar radiative effects of a Saharan dust plume observed during SAMUM assuming spheroidal model particles, Tellus B: Chemical and Physical Meteorology, 61, 270–296, https://doi.org/10.1111/j.1600-0889.2008.00389.x, 2009.

Otto, S., Trautmann, T., and Wendisch, M.: On realistic size equivalence and shape of spheroidal Saharan mineral dust particles applied in solar and thermal radiative transfer calculations, Atmospheric Chemistry and Physics, 11, 4469–4490, https://doi.org/10.5194/acp-11-4469-2011, 2011.

Painter, T. H., Deems, J. S., Belnap, J., Hamlet, A. F., Landry, C. C., and Udall, B.: Response of Colorado River runoff to dust radiative forcing in snow, Proceedings of the National Academy of Sciences, 107, 17 125–17 130, https://doi.org/10.1073/pnas.0913139107, 2010.

Pérez García-Pando, C., Thomson, M. C., Stanton, M. C., Diggle, P. J., Hopson, T., Pandya, R., Miller, R. L., and Hugonnet, S.: Meningitis and climate: from science to practice, Earth Perspectives, 1, 1–15, https://doi.org/10.1186/2194-6434-1-14, 2014.

Perlwitz, J. P., Pérez García-Pando, C., and Miller, R. L.: Predicting the mineral composition of dust aerosols – Part 1: Representing key processes, Atmospheric Chemistry and Physics, 15, 11 593–11 627, https://doi.org/10.5194/acp-15-11593-2015, 2015a.

Perlwitz, J. P., Pérez García-Pando, C., and Miller, R. L.: Predicting the mineral composition of dust aerosols – Part 2: Model evaluation and identification of key processes with observations, Atmospheric Chemistry and Physics, 15, 11 629–11 652, https://doi.org/10.5194/acp-15-11629-2015, 2015b.

Petroff, A. and Zhang, L.: Development and validation of a size-resolved particle dry deposition scheme for application in aerosol transport models, Geoscientific Model Development, 3, 753–769, https://doi.org/10.5194/gmd-3-753-2010, 2010.

Piedra, P. and Moosmüller, H.: Optical losses of photovoltaic cells due to aerosol deposition: Role of particle refractive index and size, Solar Energy, 155, 637–646, https://doi.org/10.1016/j.solener.2017.06.047, 2017.

Piskunov, V.: Parameterization of aerosol dry deposition velocities onto smooth and rough surfaces, Journal of Aerosol Science, 40, 664–679, https://doi.org/10.1016/j.jaerosci.2009.04.006, 2009.

Price, H. C., Baustian, K. J., McQuaid, J. B., Blyth, A., Bower, K. N., Choularton, T., Cotton, R. J., Cui, Z., Field, P. R., Gallagher, M., Hawker, R., Merrington, A., Miltenberger, A., Neely III, R. R., Parker, S. T., Rosenberg, P. D., Taylor, J. W., Trembath, J., Vergara-Temprado, J., Whale, T. F., Wilson, T. W., Young, G., and Murray, B. J.: Atmospheric Ice-Nucleating Particles in the Dusty Tropical Atlantic, Journal of Geophysical Research: Atmospheres, 123, 2175–2193, https://doi.org/10.1002/2017JD027560, 2018.

Prospero, J., Barrett, K., Church, T., Dentener, F., Duce, R., Galloway, J., Levy, H., Moody, J., and Quinn, P.: Atmospheric deposition of nutrients to the North Atlantic Basin, Biogeochemistry, 35, 27–73, https://doi.org/10.1007/BF02179824, 1996.

Pérez, C., Nickovic, S., Pejanovic, G., Baldasano, J. M., and Özsoy, E.: Interactive dust-radiation modeling: A step to improve weather forecasts, Journal of Geophysical Research: Atmospheres, 111, https://doi.org/10.1029/2005JD006717, 2006.

Pérez García-Pando, C., Miller, R. L., Perlwitz, J. P., Rodríguez, S., and Prospero, J. M.: Predicting the mineral composition of dust aerosols: Insights from elemental composition measured at the Izaña Observatory, Geophysical Research Letters, 43, 10,520–10,529, https://doi.org/10.1002/2016GL069873, 2016.

Querol, X., Tobías, A., Pérez, N., Karanasiou, A., Amato, F., Stafoggia, M., Pérez García-Pando, C., Ginoux, P., Forastiere, F., Gumy, S., Mudu, P., and Alastuey, A.: Monitoring the impact of desert dust outbreaks for air quality for health studies, Environment International, 130, 104 867, https://doi.org/10.1016/j.envint.2019.05.061, 2019.

Reid, E. A., Reid, J. S., Meier, M. M., Dunlap, M. R., Cliff, S. S., Broumas, A., Perry, K., and Maring, H.: Characterization of African dust transported to Puerto Rico by individual particle and size segregated bulk analysis, Journal of Geophysical Research: Atmospheres, 108, https://doi.org/10.1029/2002JD002935, 2003.

Reynolds, R. L., Cattle, S. R., Moskowitz, B. M., Goldstein, H. L., Yauk, K., Flagg, C. B., Berquó, T. S., Kokaly, R. F., Morman, S., and Breit, G. N.: Iron oxide minerals in dust of the Red Dawn event in eastern Australia, September 2009, Aeolian Research, 15, 1–13, https://doi.org/10.1016/j.aeolia.2014.02.003, 2014.

Rocha-Lima, A., Martins, J. V., Remer, L. A., Todd, M., Marsham, J. H., Engelstaedter, S., Ryder, C. L., Cavazos-Guerra, C., Artaxo, P., Colarco, P., and Washington, R.: A detailed characterization of the Saharan dust collected during the Fennec campaign in 2011: in situ ground-based and laboratory measurements, Atmospheric Chemistry and Physics, 18, 1023–1043, https://doi.org/10.5194/acp-18-1023-2018, 2018.

Rodríguez, S., Prospero, J. M., López-Darias, J., García-Alvarez, M.-I., Zuidema, P., Nava, S., Lucarelli, F., Gaston, C. J., Galindo, L., and Sosa, E.: Tracking the changes of iron solubility and air pollutants traces as African dust transits the Atlantic in the Saharan dust outbreaks, Atmospheric Environment, 246, 118 092, https://doi.org/10.1016/j.atmosenv.2020.118092, 2021.

Ryder, C. L., Marenco, F., Brooke, J. K., Estelles, V., Cotton, R., Formenti, P., McQuaid, J. B., Price, H. C., Liu, D., Ausset, P., Rosenberg, P. D., Taylor, J. W., Choularton, T., Bower, K., Coe, H., Gallagher, M., Crosier, J., Lloyd, G., Highwood, E. J., and Murray, B. J.: Coarse-mode mineral dust size distributions, composition and optical properties from AER-D aircraft measurements over the tropical eastern Atlantic, Atmospheric Chemistry and Physics, 18, 17 225–17 257, https://doi.org/10.5194/acp-18-17225-2018, 2018.

Saito, M. and Yang, P.: Advanced Bulk Optical Models Linking the Backscattering and Microphysical Properties of Mineral Dust Aerosol, Geophysical Research Letters, 48, e2021GL095 121, https://doi.org/10.1029/2021GL095121, 2021.

Sarangi, C., Qian, Y., Rittger, K., Ruby Leung, L., Chand, D., Bormann, K. J., and Painter, T. H.: Dust dominates high-altitude snow darkening and melt over high-mountain Asia, Nature Climate Change, 10, 1045–1051, https://doi.org/10.1038/s41558-020-00909-3, 2020.

Scanza, R. A., Mahowald, N., Ghan, S., Zender, C. S., Kok, J. F., Liu, X., Zhang, Y., and Albani, S.: Modeling dust as component minerals in the Community Atmosphere Model: development of framework and impact on radiative forcing, Atmospheric Chemistry and Physics, 15, 537–561, https://doi.org/10.5194/acp-15-537-2015, 2015.

Scheuvens, D., Kandler, K., Küpper, M., Lieke, K., Zorn, R., Ebert, M., Schütz, L., and Weinbruch, S.: Individual-particle analysis of airborne dust samples collected over Morocco in 2006 during SAMUM 1, Tellus B: Chemical and Physical Meteorology, 63, 512–530, https://doi.org/10.1111/j.1600-0889.2011.00554.x, 2011.

Schulz, M., Prospero, J. M., Baker, A. R., Dentener, F., Ickes, L., Liss, P. S., Mahowald, N. M., Nickovic, S., García-Pando, C. P., Rodríguez, S., Sarin, M., Tegen, I., and Duce, R. A.: Atmospheric Transport and Deposition of Mineral Dust to the Ocean: Implications for Research Needs, Environmental Science & Technology, 46, 10 390–10 404, https://doi.org/10.1021/es300073u, 2012.

Shao, Y., Wyrwoll, K.-H., Chappell, A., Huang, J., Lin, Z., McTainsh, G. H., Mikami, M., Tanaka, T. Y., Wang, X., and Yoon, S.: Dust cycle: An emerging core theme in Earth system science, Aeolian Research, 2, 181–204, https://doi.org/10.1016/j.aeolia.2011.02.001, 2011.

Shi, T., He, C., Zhang, D., Zhang, X., Niu, X., Xing, Y., Chen, Y., Cui, J., Pu, W., and Wang, X.: Opposite Effects of Mineral Dust Nonsphericity and Size on Dust-Induced Snow Albedo Reduction, Geophysical Research Letters, 49, e2022GL099 031, https://doi.org/10.1029/2022GL099031, 2022.

Sokolik, I. N. and Toon, O. B.: Incorporation of mineralogical composition into models of the radiative properties of mineral aerosol from UV to IR wavelengths, Journal of Geophysical Research: Atmospheres, 104, 9423–9444, https://doi.org/10.1029/1998JD200048, 1999.

Sokolik, I. N., Winker, D. M., Bergametti, G., Gillette, D. A., Carmichael, G., Kaufman, Y. J., Gomes, L., Schuetz, L., and Penner, J. E.: Introduction to special section: Outstanding problems in quantifying the radiative impacts of mineral dust, Journal of Geophysical Research: Atmospheres, 106, 18 015–18 027, https://doi.org/10.1029/2000JD900498, 2001.

Stockdale, A., Krom, M. D., Mortimer, R. J. G., Benning, L. G., Carslaw, K. S., Herbert, R. J., Shi, Z., Myriokefalitakis, S., Kanakidou, M., and Nenes, A.: Understanding the nature of atmospheric acid processing of mineral dusts in supplying bioavailable phosphorus to the oceans, Proceedings of the National Academy of Sciences, 113, 14 639–14 644, https://doi.org/10.1073/pnas.1608136113, 2016.

Strong, J. D. O., Vecchi, G. A., and Ginoux, P.: The Climatological Effect of Saharan Dust on Global Tropical Cyclones in a Fully Coupled GCM, Journal of Geophysical Research: Atmospheres, 123, 5538–5559, https://doi.org/10.1029/2017JD027808, 2018.

Textor, C., Schulz, M., Guibert, S., Kinne, S., Balkanski, Y., Bauer, S., Berntsen, T., Berglen, T., Boucher, O., Chin, M., Dentener, F., Diehl, T., Easter, R., Feichter, H., Fillmore, D., Ghan, S., Ginoux, P., Gong, S., Grini, A., Hendricks, J., Horowitz, L., Huang, P., Isaksen, I., Iversen, I., Kloster, S., Koch, D., Kirkevåg, A., Kristjansson, J. E., Krol, M., Lauer, A., Lamarque, J. F., Liu, X., Montanaro, V., Myhre, G., Penner, J., Pitari, G., Reddy, S., Seland, Ø., Stier, P., Takemura, T., and Tie, X.: Analysis and quantification of the diversities of aerosol life cycles within AeroCom, Atmospheric Chemistry and Physics, 6, 1777–1813, https://doi.org/10.5194/acp-6-1777-2006, 2006.

Valentin, C. and Bresson, L.-M.: Morphology, genesis and classification of surface crusts in loamy and sandy soils, Geoderma, 55, 225–245, https://doi.org/10.1016/0016-7061(92)90085-L, 1992.

van der Does, M., Knippertz, P., Zschenderlein, P., Harrison, R. G., and Stuut, J.-B. W.: The mysterious long-range transport of giant mineral dust particles, Science Advances, 4, eaau2768, https://doi.org/10.1126/sciadv.aau2768, 2018.

Vasiliou, J. G., Sorensen, D., and McMurry, P. H.: Sampling at controlled relative humidity with a cascade impactor, Atmospheric Environment, 33, 1049–1056, https://doi.org/10.1016/S1352-2310(98)00323-9, 1999.

Waza, A., Schneiders, K., May, J., Rodríguez, S., Epple, B., and Kandler, K.: Field comparison of dry deposition samplers for collection of atmospheric mineral dust: results from single-particle characterization, Atmospheric Measurement Techniques, 12, 6647–6665, https://doi.org/10.5194/amt-12-6647-2019, 2019.

Welti, A., Lohmann, U., and Kanji, Z. A.: Ice nucleation properties of K-feldspar polymorphs and plagioclase feldspars, Atmospheric Chemistry and Physics, 19, 10 901–10 918, https://doi.org/10.5194/acp-19-10901-2019, 2019.

Yang, W., Marshak, A., Kostinski, A. B., and Várnai, T.: Shape-induced gravitational sorting of Saharan dust during transatlantic voyage: Evidence from CALIOP lidar depolarization measurements, Geophysical Research Letters, 40, 3281–3286, https://doi.org/10.1002/grl.50603, 2013.

Yu, H., Chin, M., Yuan, T., Bian, H., Remer, L. A., Prospero, J. M., Omar, A., Winker, D., Yang, Y., Zhang, Y., Zhang, Z., and Zhao, C.: The fertilizing role of African dust in the Amazon rainforest: A first multiyear assessment based on data from Cloud-Aerosol Lidar and Infrared Pathfinder Satellite Observations, Geophysical Research Letters, 42, 1984–1991, https://doi.org/10.1002/2015GL063040, 2015.

Yun, J., Link, N., Kumar, A., Shchukarev, A., Davidson, J., Lam, A., Walters, C., Xi, Y., Boily, J.-F., and Bertram, A. K.: Surface Composition Dependence on the Ice Nucleating Ability of Potassium-Rich Feldspar, ACS Earth and Space Chemistry, 4, 873–881, https://doi.org/10.1021/acsearthspacechem.0c00077, 2020.

Yus-Díez, J., Pandolfi, M., González-Flórez, C., Escribano, J., Gonzalez-Romero, J., Ivančič, M., Rigler, M., Klose, M., Kandler, K., Panta, A., Querol, X., Reche, C., Perez García-Pando, C., and Alastuey, A.: Quantifying variations in multi-wavelength optical properties of freshly-emitted Saharan dust from the Lower Drâa Valley, Moroccan Sahara, in prep.

Zhang, X. L., Wu, G. J., Zhang, C. L., Xu, T. L., and Zhou, Q. Q.: What is the real role of iron oxides in the optical properties of dust aerosols?, Atmospheric Chemistry and Physics, 15, 12 159–12 177, https://doi.org/10.5194/acp-15-12159-2015, 2015.

Zimmermann, F., Weinbruch, S., Schütz, L., Hofmann, H., Ebert, M., Kandler, K., and Worringen, A.: Ice nucleation properties of the most abundant mineral dust phases, Journal of Geophysical Research: Atmospheres, 113, https://doi.org/10.1029/2008JD010655, 2008.